



Peter Adrian LEITL, Dipl.-Ing.

CFD Modelling of Air Flow Through a Paper Web from Micro-Computed Tomography (μ -CT) Data

Master's Thesis

to achieve the university degree of

Master of Science

Master's degree programme: Chemical and Process Engineering

submitted to

Graz University of Technology

Supervisor

Univ.-Prof. Dipl.-Ing. Dr.techn. Ulrich Hirn

Institute of Paper, Pulp and Fibre Technology
Head: Univ.-Prof. Dipl.-Ing. Dr.techn. Wolfgang Bauer

Graz, 2019

Affidavit

I declare that I have authored this thesis independently, that I have not used other than the declared sources/resources, and that I have explicitly indicated all material which has been quoted either literally or by content from the sources used. The text document uploaded to TUGRAZonline is identical to the present master's thesis.

Date

Signature

Thanks

I would like to take the opportunity to thank Univ-Prof. Ulrich Hirn for the supervision of this master's thesis at the Institute of Paper, Pulp and Fibre Technology.

My thanks also go to Dr. Karin Zojer and Dr. Eduardo Machado from the Institute of Solid State Physics for especially supporting the material analyses and to the company Bionic Surface Technologies GmbH for providing the required software and hardware. Furthermore, my thanks go to Univ.-Prof. Wolfgang Bauer, who has aroused my interest in paper and pulp technologies in numerous courses.

The incentive to carry out this work resulted from my more than ten year old experience in using CFD to solve different problems. Increasing the knowledge in different fields of science is important for succeeding with an engineering company. This was also a big motivational factor to finish the second master's thesis.

My special thanks also go to my entire family and friends, who have always provided me with the necessary support during my studies.

Dipl.-Ing. Peter Adrian Leitl Graz, January 2020

Abstract

A paper web sample was scanned using μ -CT. This produces a dataset of images in .tif format. From these images a 3D geometry was generated using Fiji, which is an image processing software. Based on the 3D geometry of the fibre material, a volume mesh generation process was started, meshing the air volume between the fibre material and some extra volume above and under the paper web. This volume mesh was used for the CFD (computation fluid dynamics) analyses. In the CFD simulation the air flow through the pores in the paper web was calculated. Gurley measurement results are available to evaluate the CFD calculations. The sample of the paper web has a total length of 2.8mm and a width of 2.0mm. Since the resolution of the μ -CT used was $1.5\mu\text{m}$ it was required to split the sample in 4×3 single segments for the CFD simulation. Each of these segments was analysed. The total thickness of the volume is 0.167mm the first and the last section of this volume is air (0.04mm). The paper web including the pores is placed in between. Since the material is anisotropic the thickness of the paper web varies between 0.04mm and 0.12mm.

Different methods of segmentation for geometry creation have been studied and result in different average flow rates. The difference between the single segments is constant, comparing the flow results of the different segmentation methods. The final segmentation is used for post processing, the other segmentation result shows unrealistic holes in the single fibres. A comparison of the final segmentation CFD result and the Gurley measurement shows that the average flow rate of the simulation is 4.2 times the measured flow rate. Since the area used in the Gurley measurement is 1780 times bigger than the sample size used in the CFD simulation, a difference between the two methods can be expected. The smallest flow rate in the simulation is 1.88 times the average of the measured flow rate. The biggest one is 7.16 times the measured flow rate. Analysing the flow rate in detail,

it is obvious that the big pores are the main reason for the different flow rates of the single sections.

A new analysis method will be introduced, using an iso-volume of the total pressure in combination with a minimum air speed (the entropy has to be used instead of the total pressure, if the fluid is modelled as an ideal gas and changes in the density appearance). Firstly, the pores in the paper web are marked, secondly, the minimum velocity marks only the pores which see an airflow. With this method it is possible to visualise the pores and in a second step it is possible to visualise the volume of the pores, which are responsible for the flow rate through the paper web. The result shows that 50% of the flow goes through less than 1.4% of the sample area of the investigated paper web. The flow field is very anisotropic which means most of the air goes through a small amount of pores.

For all simulations the CFD Solver of the commercial software Ansys Fluent has been used. Simple calculations show that the flow is laminar, so the laminar flow model in Fluent has been used in combination with a steady solver. The air has been modelled using the law of ideal gas.

Contents

Abstract	iv
1 Introduction	1
2 Air Resistance of Paper (Gurley Method)	4
2.1 Paper Web	5
2.2 Gurley Method Results	6
3 Geometry Creation using μ-CT data	8
3.1 Images Basis Segmentation	11
3.2 Images 3 x Scaled Segmentation	12
3.3 Images 5 x Scaled Segmentation	13
3.4 3D Geometry and differences caused by the Segmentation Methods	15
3.4.1 3D Geometry Basis Segmentation	17
3.4.2 3D Geometry 3 x Scaled Segmentation	18
3.4.3 3D Geometry 5 x Scaled Segmentation	19
3.4.4 Conclusion of the Segmentation Methods	20
4 Mesh Creation	21
4.1 Basis mesh	23
4.2 Double resolution mesh	26
5 Solver and Boundary Conditions	29
5.1 Computational Fluid Dynamics CFD	29
5.1.1 Basic Equations of Fluid Mechanics	29
5.1.2 Discretization	31
5.1.3 Finite-Volume Methods (FVM)	31
5.2 Gurley Boundary Conditions	32

Contents

5.3	Process Boundary Conditions	33
5.4	Analytical Estimations	33
6	Effect of Segmentation Method and Mesh Resolution	36
6.1	Effect of Segmentation	36
6.2	Influence of the Mesh Resolution on the Flow Rate	39
7	Results of the total Sample (3 x 4 Segments)	41
7.1	Basis Segmentation Results	41
7.2	5 x Scaled Segmentation Results	43
7.3	5 x Scaled Segmentation Results at Process Boundary Conditions (5bar)	45
7.4	Comparison of the Segmentation Methods	47
7.5	Comparison of the Measurement Results and the 5 x Scaled Segmentation Result	49
8	Porosity	50
8.1	Introduction of porosity calculation using Iso-Surfaces	50
8.2	Porosity Results using Iso-Volumes of the Total Pressure	53
8.3	Comparison of the Results with Carman-Kozeny-Equation	59
9	Results of S3 R1 in Detail	62
10	Conclusion	71
	Bibliography	72

List of Figures

2.1	Principle sketch and Gurley densometer with optional 4320 programmable digital timer token from: http://www.saurashtra.net/Packaging-And-Material-Testing-Equipments	5
2.2	Microscope image of the investigated paper web, (a) and (b) show exactly the same region of the paper	6
3.1	Original μ -CT data full size	8
3.2	Original μ -CT data in the detail	9
3.3	Workflow for geometry and mesh creation	10
3.4	Example of the first four .tif images used for geometry build up	11
3.5	Example of the first four .tif images created with the 3 x scaling method	12
3.6	Example of the first two .tif images created with the 5 x scaling method	13
3.7	Comparison of the geometries created by the different scaling methods	14
3.8	12 segments of the paper web	15
3.9	S3 R1 in detail, height of the fibres scaled with a factor of two in μm	16
3.10	S3 R1 in detail, height of the fibres scaled with a factor of two in μm and the lower regions removed	16
3.11	S3 R1 basis segmentation	17
3.12	S3 R1 3 x scaled segmentation	18
3.13	S3 R1 5 x scaled segmentation	19
4.1	Volume elements used for creating CFD meshes	23
4.2	Scaled and meshed geometry	24
4.3	Mesh in original size of the μ -CT scan resolving all gaps between fibres	24

List of Figures

4.4	Basis mesh in original size	25
4.5	Eight times finer mesh	26
4.6	Four times finer mesh	27
5.1	Sketch of the boundary conditions for the Gurley measurement	32
5.2	Sketch of the boundary conditions, for industrial filling of the sacks	33
6.1	Resulting geometry (left) and CFD result (right) in detail, showing some holes	36
6.2	Basis segmentation, showing many holes	37
6.3	3 x scaled segmentation, showing some holes	37
6.4	5 x scaled segmentation, showing less holes	38
7.1	CFD Result of all 12 segments using the basis segmentation .	41
7.2	CFD Result of all 12 segments using the 5 x scaling method .	43
7.3	CFD Result of all 12 segments using the 5 x scaling method at 5 bar pressure difference	46
7.4	Basis scaling method, normalized flow rate	47
7.5	5 x scaling method, normalized flow rate	47
7.6	Difference between normalized flow rates in percent	48
7.7	Comparison measurement vs. CFD	49
8.1	Total pressure though the sample, the black lines show the total pressure iso-lines	52
8.2	Volume fractions identified for $p_{tot} \leq 12.2[Pa]$ (Bottom Vol- ume) and $1207.8[Pa] \leq p_{tot}$ (Top Volume)	52
8.3	Comparison of the normalized porosity with the normalized flow rate	54
8.4	S3 R1 Top side y-coordinate [μm]	55
8.5	S3 R1 top side y-coordinate [μm] of the iso volume for calcu- lation of the porosity	56
8.6	Detail of the total pressure iso-surface, pore detection mecha- nism	57
8.7	S3 R1 top side y-coordinate of the pores [μm]	58
8.8	S3 R1 top side y-coordinate of the pores [μm]	61
9.1	CFD Result S3 R1 stream lines through the paper web top view	62

List of Figures

9.2	CFD Result S3 R1 stream lines through the paper web bottom view	63
9.3	Stream lines, coloured with the y coordinate in [μm] through the paper web	64
9.4	Static pressure in the z-plane	65
9.5	Velocity in the z-plane	65
9.6	All pores in the middle of the paper web	66
9.7	Secondary flow velocity in the pores	67
9.8	Pores responsible for 50% of the flow rate in the middle of the paper web	68
9.9	Flow rate depending on the pore area	70

List of Tables

2.1	Measurement results sack kraft paper	7
4.1	Estimation Mesh Size	22
5.1	Estimation Reynolds number for Gurley boundary conditions	34
5.2	Estimation Reynolds number for process boundary conditions	34
5.3	Estimation Mach number for different boundary conditions .	35
6.1	Results of different segmentation methods in comparison to the measurement	39
6.2	Results of different meshing methods for the basis segmentation	40
7.1	Basis segmentation simulation results sack kraft paper	42
7.2	5 x scaled segmentation simulation results sack kraft paper .	44
7.3	5 x scaled segmentation simulation results sack kraft paper .	45
8.1	Porosity for 5x segmentation simulation results	53
8.2	Porosity for 5x segmentation simulation results	60
9.1	Pore analyses, area and area weighted velocity	69

1 Introduction

The production of paper bags used for cement or powder flour is challenging, especially in terms of porosity. The pores should be fine enough so that no powder goes through the paper web. However, they should also be large enough that the air used to fill the powdered goods to the sack can pass through the pores during the filling process of the bag. The fibres in a paper are randomly distributed, hence, producing big and small pores. For measuring the porosity in the paper web different methods can be used. The most common methods are the Bendtsen or Gurley air permeability measurement (TAPPI T 460 m49, ASTM D-726-58/Method A and ISO 5636/5) see also [Kna86].

The advantage of the Gurley method is its simplicity. It is used to measure the air resistance of a circular area of paper using a pressure differential. The measurement results for the used paper are discussed in chapter 2. The disadvantage of the method is that the value contains no information about pore size, size distribution and the uniformity of the distribution of the pores.

In order to study the interactions between pore structure and fluids, a common approved method is Micro-Computed Tomography (μ -CT). [Asl17] studied uncoated paper using μ -CT with a resolution of $0.9\mu m$ and did optical measurements of the water penetration into paper using confocal laser scanning microscopy. They used the μ -CT for calculating the porosity and pore size distribution.

Other authors like [Aalo4] use μ -CT for geometry creation and lattice-Boltzmann flow simulations for analysing the flow in fibrous materials. The Lattice-Boltzmann method is based on the calculation of particle micro dynamics.

1 Introduction

[Mac18] et al. introduced a powerful segmentation method and analysed the paper structure like thickness, porosity, fractions of externally accessible pores and mean geodesic tortuosity using the rolling ball approach. One challenge they worked out is that the thickness and porosity values extracted from the microstructure strongly depend on the actual definition of the paper surface.

In this work, a new method is introduced using the total pressure isobars for the definition of the paper web surface. These results can be used for calculating the fluid relevant porosity. Also, the most relevant pores responsible for the air flow through the paper can be identified with these simulations. Therefore, computational fluid dynamics (CFD) is used for analysing the flow field through the paper web. In this numerical method the fluid volume is discretised in small sub elements. In these sub elements (CFD mesh) the Navier Stokes equations can be solved using numerical codes which secure the conservation of mass, impulse and energy. The mesh may have any tetrahedral, hexahedron, pyramid, wedge, polygonal or polyhedral shape. That's why complicated geometries like the air volume around a paper network structure can be meshed and simulated. The solution of the unknown variables (eg. velocity, pressure and temperature) occurs at the midpoints or at the nodes of these finite volumes [ANS13]. CFD simulations are used in many different fields of science and industrial applications. Over the last decades the computational power has increased a lot, that is one reason why CFD applications are entering more and more fields.

Aim of the work: one important purpose is the evaluation of the segmentation method. Three different segmentation methods are evaluated in this work. The segmentation method uses μ -CT data and converts it into binary data (two different pixel colours). Black represents air volume and white represents fibre material. These image sets are converted to a 3D geometry, which is used for the meshing process. Since the meshing process and the solver setup for the CFD simulation are always similar, the only changing variable is the segmentation method. The CFD results can be compared with Gurley measurements of the same paper. The segmentation method, which delivers the most accurate results in comparison to the measurement, is then used for the final flow field and porosity analyses.

1 Introduction

Outline of the thesis: The segmentation method has a major influence on the resulting porosity and the flow field. The basis segmentation creates unrealistic holes in the fibre material, these holes are responsible for 7 times bigger flow rates through the paper in comparison to the measurement. The final segmentation method closes these holes and results in a flow rate only four times the measured average. Another important outcome of the work is the required CFD mesh setup. Since the pixel size of the binary data is $1.5\mu\text{m}$ the smallest length of the CFD mesh has to be the same length or smaller to fully resolve the geometry. To work with a data set with a maximum volume of $2.8\text{mm} \times 2\text{mm} \times 0.167\text{mm}$ and a smallest length of $1.5\mu\text{m}$ it was required to split the dataset into twelve separate segments. To reduce the size of the mesh (amount of nodes in the mesh $1.44 \cdot 10^7$) a scaling trick was used. This process results in a proper mapping of the 3D geometry. These segments can be simulated on a standard CFD workstation (12 CPUs and 132 GB RAM). A CFD mesh study outlines that an eight times bigger mesh ($1.15 \cdot 10^8$ nodes, called "double resolution mesh") gives an increase in the flow rate to the basis method of 8% to 17%, depending on the paper segment. The disadvantage of the double resolution mesh is the usability. Since the double resolution mesh requires enormous amounts of computational power and RAM (simulation only on a CFD cluster) and the influence of the segmentation method is much bigger, the basis meshing method was used for all analyses.

2 Air Resistance of Paper (Gurley Method)

The Gurley method [Kna86] is used to measure the air resistance of an approximately 6.45cm^2 circular area of paper using a pressure differential of 1.22kPa . It measures the time necessary to press 100ml of air through the paper. The recommended range of the instrument is from 5 to 1800 seconds per 100ml air. For more impermeable papers, the time requirements become so excessive that other techniques are preferable. This method measures the volume of air that passes through the tested paper web along with possible leakage of air parallel to the paper plane. In the current study the measurements have been taken at the Institute of Paper, Pulp and Fibre Technology. Figure 2.1 shows a typical Gurley densometer used for resistance measurement. The measurement itself is simple. The paper is placed at the bottom part of the device, then the bottom part closes and the measurement starts. The measured time (Gurley time) value does not give information about, how the air goes through the pores or how the pores are distributed, so there can be either few big pores or many small pores which both can create the same result. Still, the Gurley method is well known and widely used in the paper and pulp industry for testing air permeability of paper.

2 Air Resistance of Paper (Gurley Method)

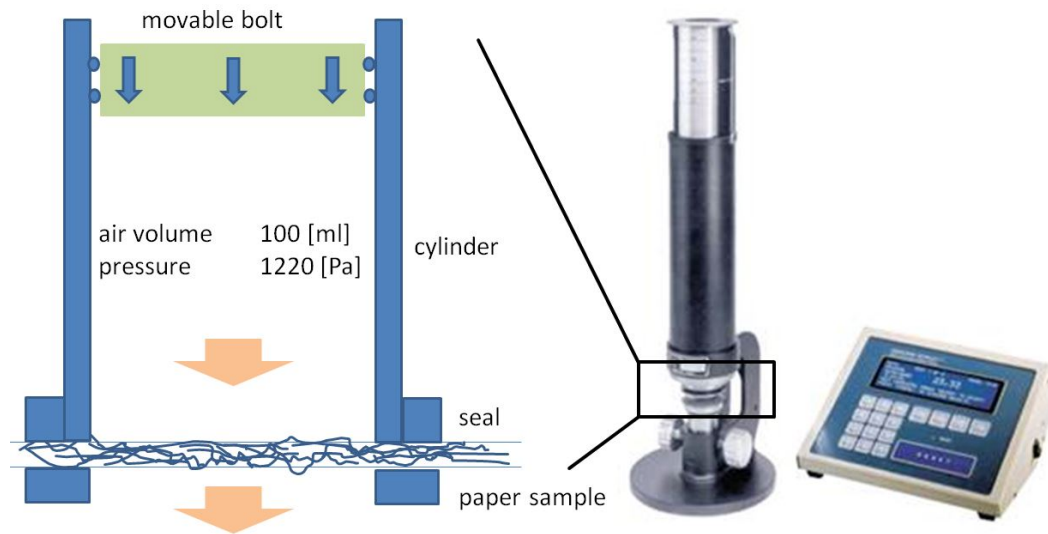


Figure 2.1: Principle sketch and Gurley densometer with optional 4320 programmable digital timer token from: <http://www.saurashtra.net/Packaging-And-Material-Testing-Equipments>

2.1 Paper Web

The paper web examined in this work is a sack kraft paper. This paper is widely used for cement bags and flour powder bags. *Figure 2.2a* provides different details about the paper surface imaged in a light microscope with top light. *Figure 2.2b* shows the same region with bottom light. The scale in both pictures has a total length of 1mm . The 12 squares are similar to the areas that are simulated with CFD. One big pore is clearly visible in the centre (black dot *Figure 2.2a*, bright dot *Figure 2.2b*). Having a look at the pictures it appears that there are regions which might be completely closed. The pictures also show that the simulated area is small. So if a hole, as it can be seen in the pictures, would be in the investigated region, the CFD simulated flow rate in that zone will be very much bigger than in the other regions.

2 Air Resistance of Paper (Gurley Method)

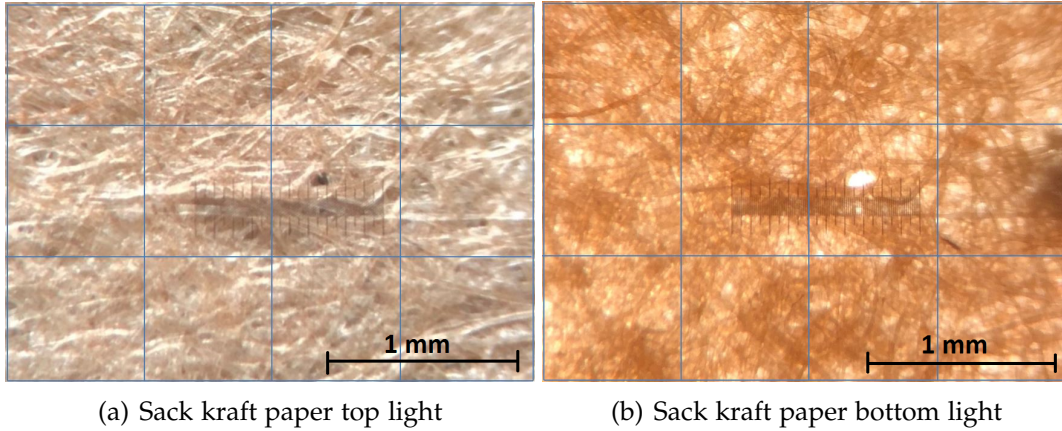


Figure 2.2: Microscope image of the investigated paper web, (a) and (b) show exactly the same region of the paper

2.2 Gurley Method Results

10 different regions of one A4 paper sample were measured using the Gurley method. This is the same paper which was imaged in the μ -CT. The results in detail can be seen in Table 2.1. The table contains each measured value, the according velocity of each value and the average AV , the standard deviation STD , the minimum value Min and the maximum measured value Max . The average measured time is $6.82sec$. Knowing the air volume which goes through the paper, the mean air velocity can be calculated using Equation 2.1. v is the mean air velocity in m/s , V the volume ($100ml$) and t the measured time in sec . The resulting velocity is $0.023m/s$. These values are later used for comparison with the CFD results.

$$v = \frac{V}{t} \quad (2.1)$$

2 Air Resistance of Paper (Gurley Method)

Table 2.1: Measurement results sack kraft paper

Name	time [s]	velocity [m/s]
1	7.6	0.0204
2	6.4	0.0242
3	6.7	0.0231
4	6.5	0.0238
5	7.7	0.0201
6	5.1	0.0304
7	7.2	0.0215
8	7.2	0.0215
9	7.1	0.0218
10	6.7	0.0231
AV	6.82	0.0230
STD	0.747	0.0029
Min	5.1	0.0201
Max	7.7	0.0304

3 Geometry Creation using μ -CT data

X-ray tomography (CT) is a well known method in medicine to picture the inner structure of the human body [Mac10]. μ -CT is the same method as used in medicine, but the system is smaller and has a greatly increased resolution. It is actually a 3D microscopy method, in which the internal structure of objects is displayed non-destructively as a stack of images with very fine resolution [Shi14]. In the present study, the resolution of one voxel (volume element for geometry description) represents a volume of $1.5 \times 1.5 \times 1.5 \mu m^3$. A mathematical algorithm was used to generate a geometry based on the μ -CT data. Original images of the paper web using μ -CT can be seen in Figure 3.1 and some more details in Figure 3.2.

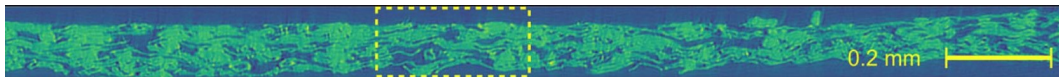


Figure 3.1: Original μ -CT data full size

3 Geometry Creation using μ -CT data

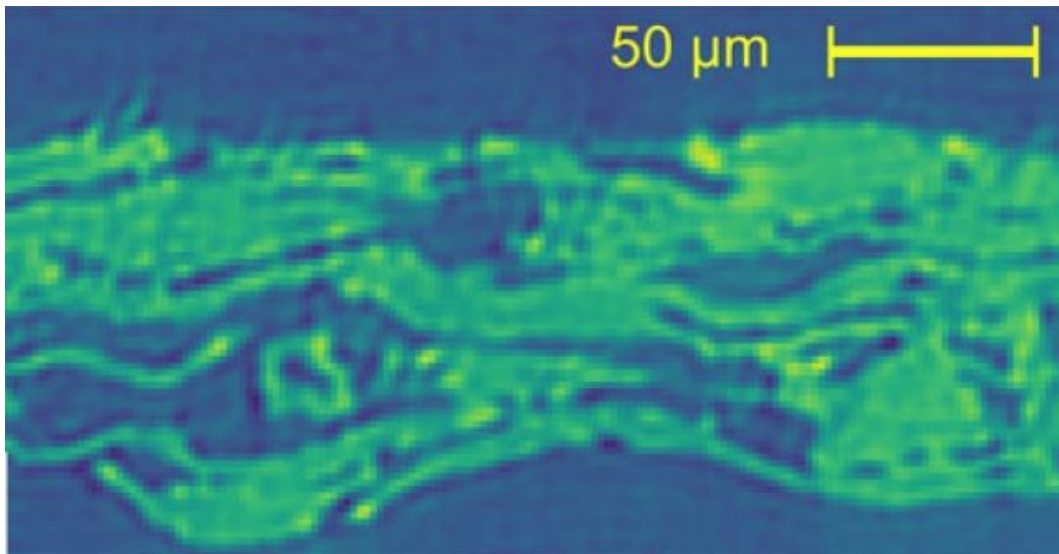


Figure 3.2: Original μ -CT data in the detail

For geometry creation a binarized μ -CT dataset is required. This can be achieved using different methods. Many details as the data segmentation procedure can be found in the detailed description in [Mac18]. In this work, three different geometry creation methods are compared. All of them are based in the segmentation which has been used in [Mac18]. The workflow to create a geometry can be seen in Figure 3.3. A detailed comparison of the resulting geometries is shown later.

3 Geometry Creation using μ -CT data

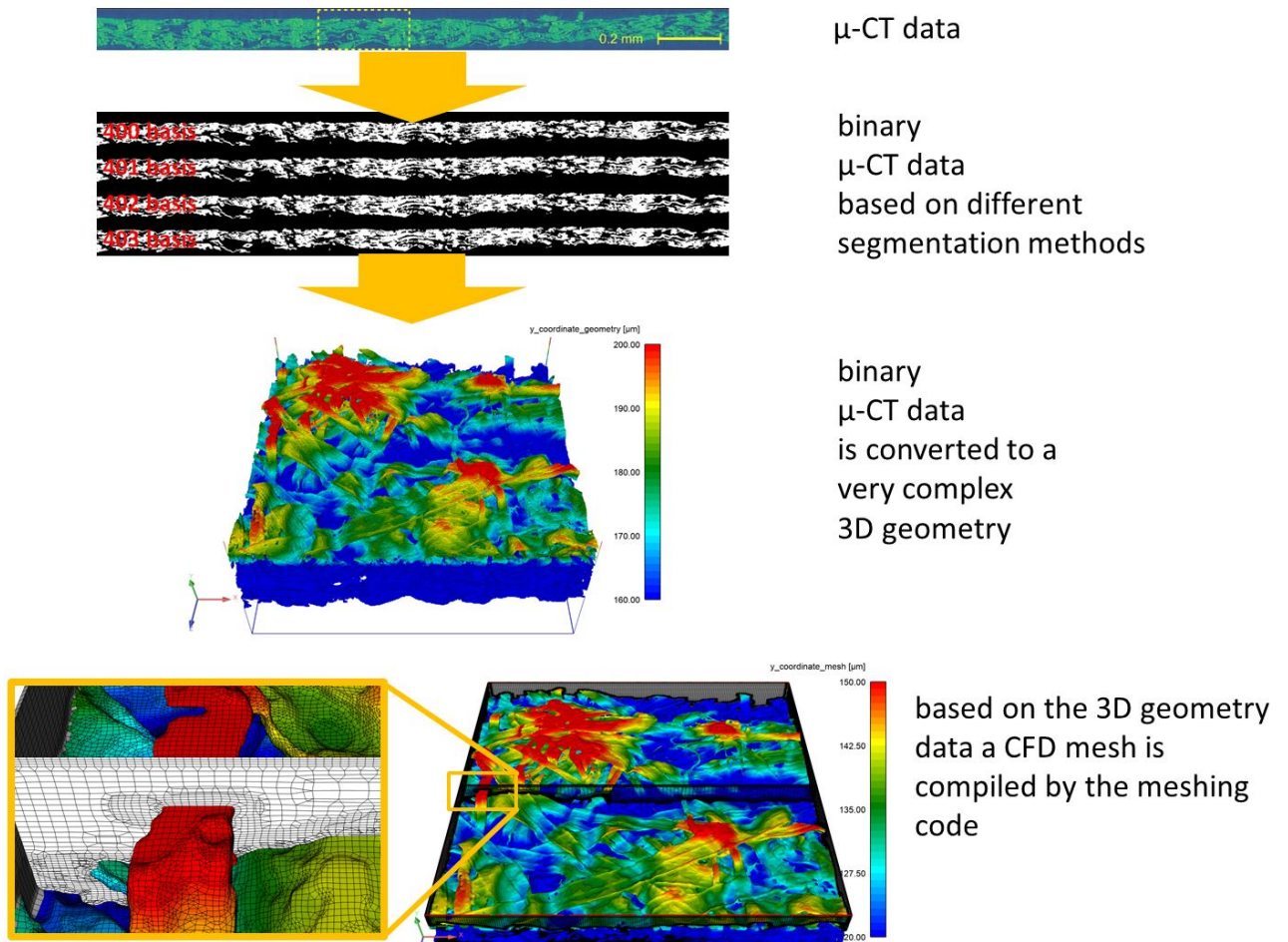


Figure 3.3: Workflow for geometry and mesh creation

3.1 Images Basis Segmentation

The basis segmentation creates the geometry in a symmetric way, so for the result if the pixel is solid or not solid, five pixels in a sphere around the target pixel are taken into account.

Figure 3.4 shows the first 4 images. One image has a length of 1875 pixels and a height of 111 pixels. A total amount of 1334 images are used. The distance between two images is $1.5\mu m$, one voxel contains the volume of $1.5\mu m^3$. The total volume used in the μ -CT is $2812.5\mu m \cdot 2001\mu m \cdot 166.5\mu m$. Fiji was used to open the produced image sequence. Fiji is an image processing package that can be used for creating 3D objects in the format .obj [19].

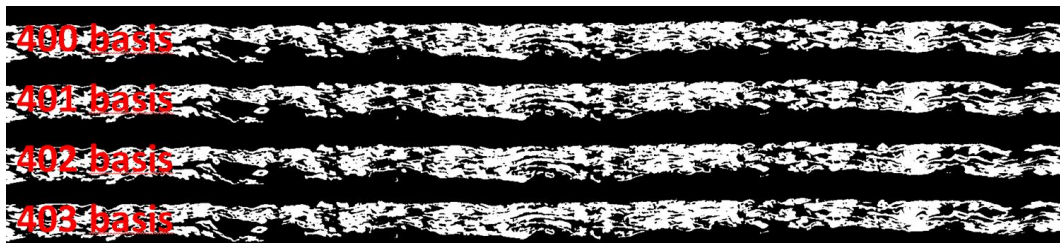


Figure 3.4: Example of the first four .tif images used for geometry build up

3.2 Images 3 x Scaled Segmentation

Since paper web is a very anisotropic material the idea was born to also run asymmetric segmentations. This can be done in a way that the mathematics used in [Mac18] stay the same but the basis images are scaled by a factor of 3 in paper thickness direction. Figure 3.5 shows the same images as Figure 3.4 just created using the different segmentation method.

Figure 3.5 shows the first 4 images. One image has a length of 1875 pixels and a height of 333 pixels (three times the basis height). As a result of the scaling more holes in the horizontal direction are closed.

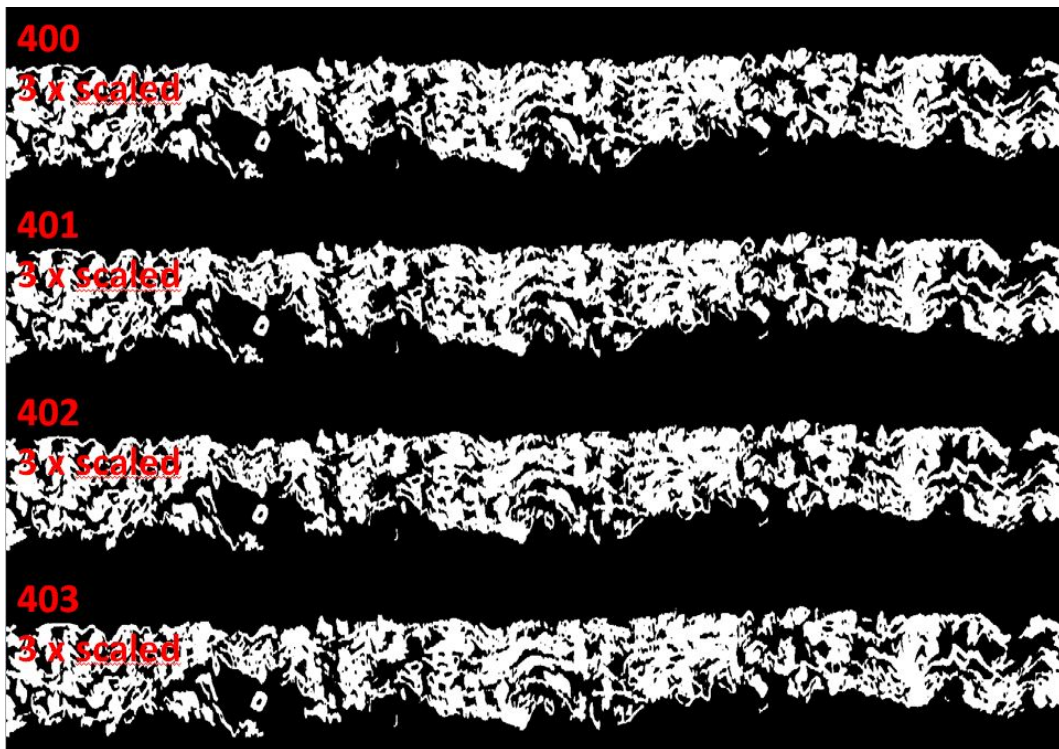


Figure 3.5: Example of the first four .tif images created with the 3 x scaling method

3.3 Images 5 x Scaled Segmentation

In this section the same method as in 3.2 has been used with the difference that the basis images have been scaled using the factor 5 in paper thickness direction. Figure 3.6 shows the first 2 images as Figure 3.4 just created using the different segmentation method.

One image has a length of 1875 pixels and a height of 555 pixels (five times the basis height). As a result of the scaling even more holes in the horizontal direction are closed than in the 3 x scaled segmentation. Since the web is very anisotropic this scaling trick can be an important tool to generate realistic geometries and air resistant results. The scaling method tuned out to be an effective technique to remove artefact holes from the segmented structure.



Figure 3.6: Example of the first two .tif images created with the 5 x scaling method

3 Geometry Creation using μ -CT data

The Figure 3.7 shows three segment geometries in comparison. All are directly created from the binary data. In section 3.4 the comparison of the geometries will be done based on hole detection, therefore all of them have the same thickness (preparation for meshing process), which is the double thickness than the paper web has in original.

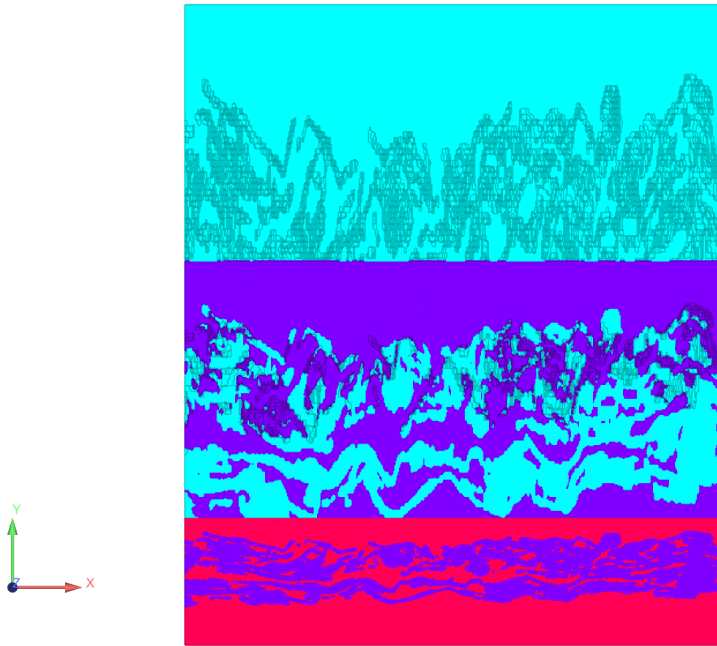


Figure 3.7: Comparison of the geometries created by the different scaling methods

3.4 3D Geometry and differences caused by the Segmentation Methods

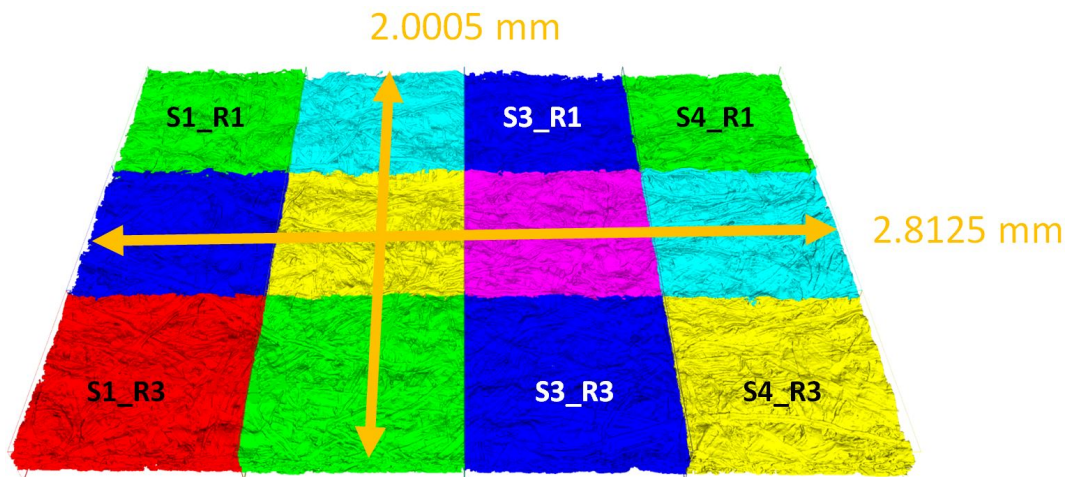


Figure 3.8: 12 segments of the paper web

It is important to build up a geometry without any filter or smoothing process to keep the accuracy as big as possible. In Fiji the image sequence was cut into $4 \times 3 = 12$ segments, because the entire dataset couldn't be processed with the hardware available (chapter 4). Each of the segments was exported after inverting the volume (subtracting the fibre material from the air volume). For CFD simulations the air fluid volume is used, with the inversion it is possible to change the material point to the air volume. The resulting 12 air volumes (Figure 3.8) are used for the meshing process. Figure 3.9 shows many details, the colour of the paper web gives the y-coordinate which is the height of the geometry. Red is at $200\mu m$, green at $180\mu m$ and blue at $160\mu m$. This image may help to understand how the paper web is built up by the single fibres. The image shows the geometry before the meshing process, that means the geometry is in y-direction scaled with a factor of two.

3 Geometry Creation using μ -CT data

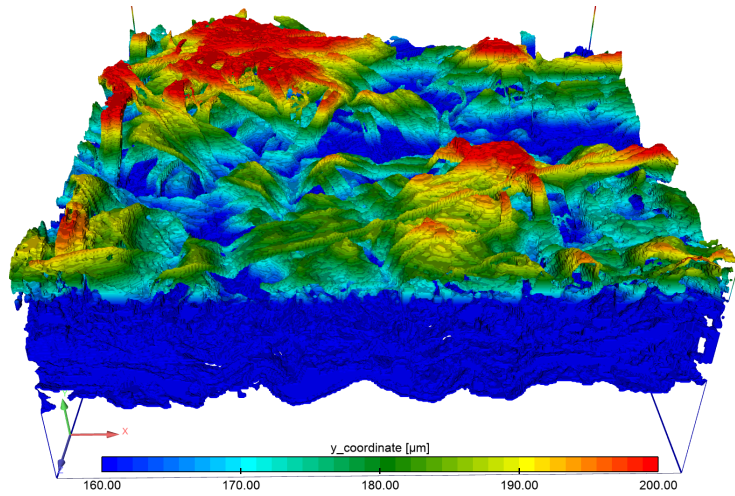


Figure 3.9: S3 R1 in detail, height of the fibres scaled with a factor of two in μm

The following section compares the geometries of the paper samples created by the different segmentation methods. The images are coloured using the y- coordinate in μm . The following images show only the geometry from $200\mu m$ to $160\mu m$. This is the top layer of the fiber material which allows to see the difference in single fibres Figure 3.10.

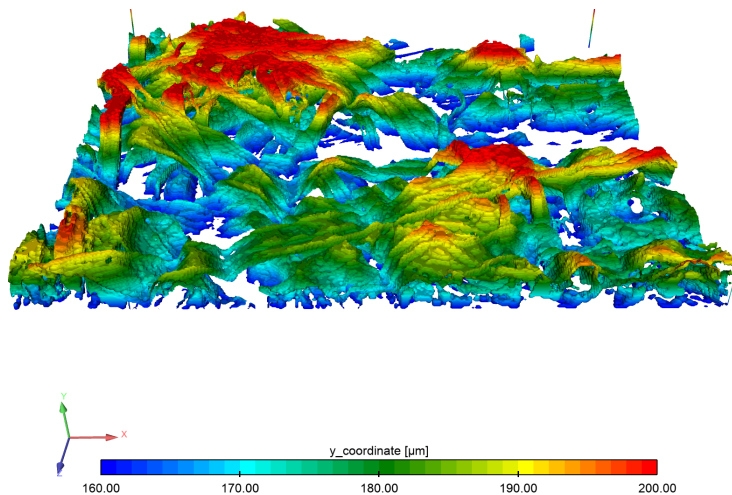


Figure 3.10: S3 R1 in detail, height of the fibres scaled with a factor of two in μm and the lower regions removed

3.4.1 3D Geometry Basis Segmentation

The basis segmentation shows many holes in the fibres. Many of the holes are in a place where the fibres have been pressed to a thin layer. This can be a reason why the symmetric segmentation method fails for these zones. The zone inside the black ellipse allows the comparison of a thin fibre zone.

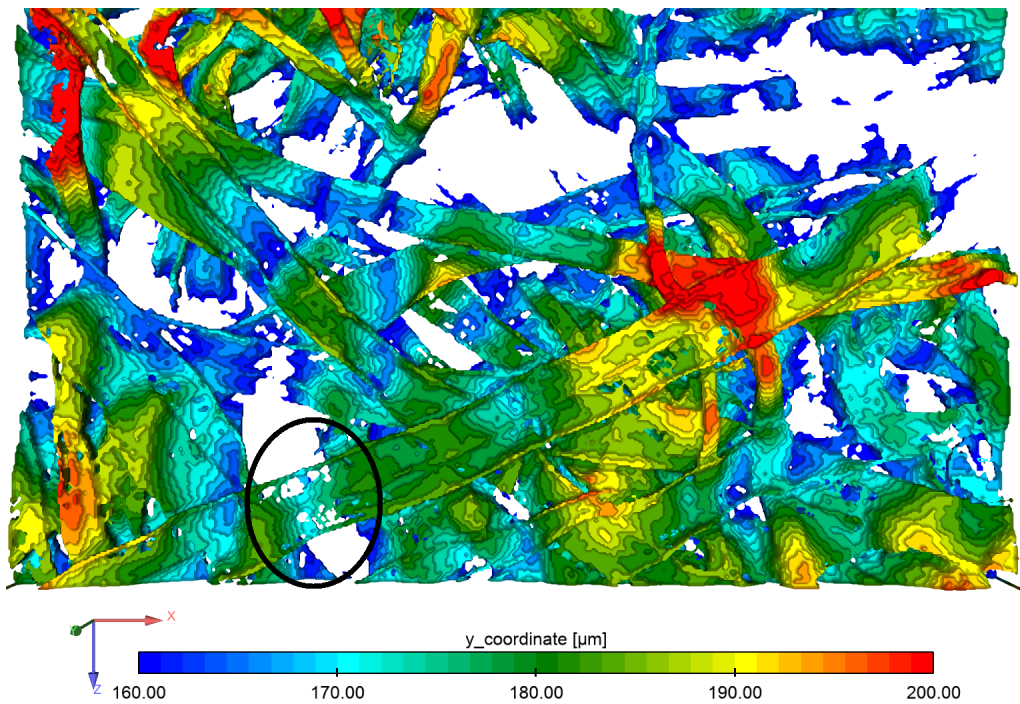


Figure 3.11: S3 R1 basis segmentation

3 Geometry Creation using μ -CT data

3.4.2 3D Geometry 3 x Scaled Segmentation

The 3 x scaled segmentation method results in a geometry with less holes in the fibre material. This can be clearly seen, especially in the long fibre starting at the left bottom of and ending at the right top of the image. The zone inside the black ellipse allows the comparison of a thin fibre zone.

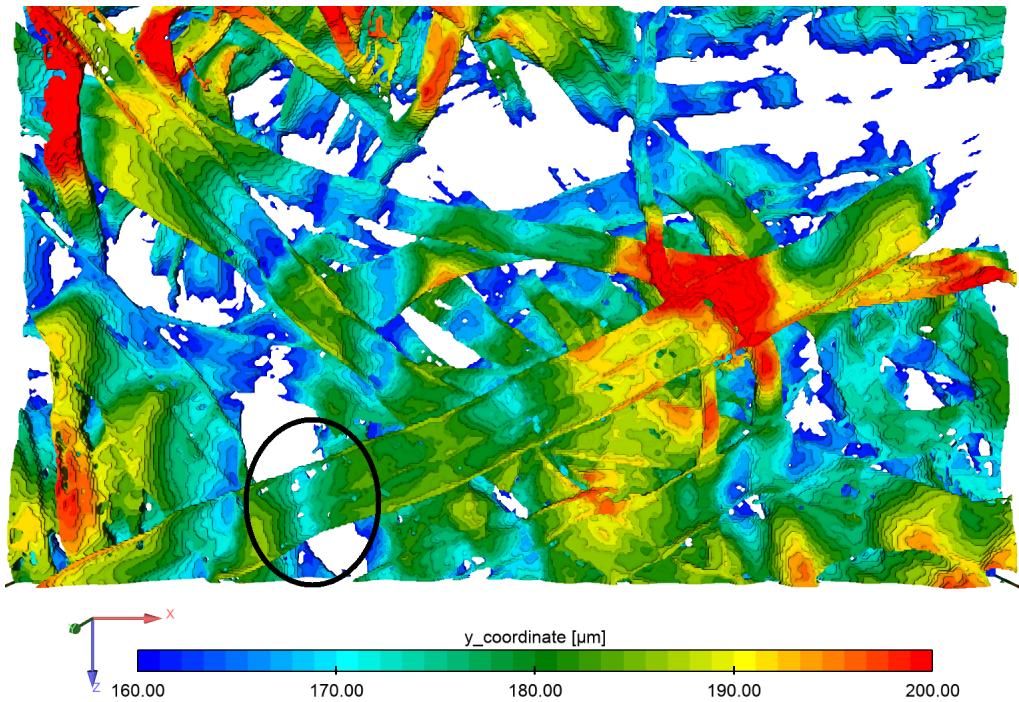


Figure 3.12: S3 R1 3 x scaled segmentation

3.4.3 3D Geometry 5 x Scaled Segmentation

The 5 x scaled segmentation method results in the smallest amount of holes in the very thin fibres. Since the segmentation method ([Mac18]) takes 5 pixels into account for calculating the border between fibre material and air, the 5 x scaled segmentation method is the maximum amount of scaling that has an effect on the image segmentations. The zone inside the black ellipse allows the comparison of a thin fibre zone. The 5 x scaled segmentation shows only small differences in comparison to the 3 x scaled method, the difference in the flow rates can be seen in chapter 6.

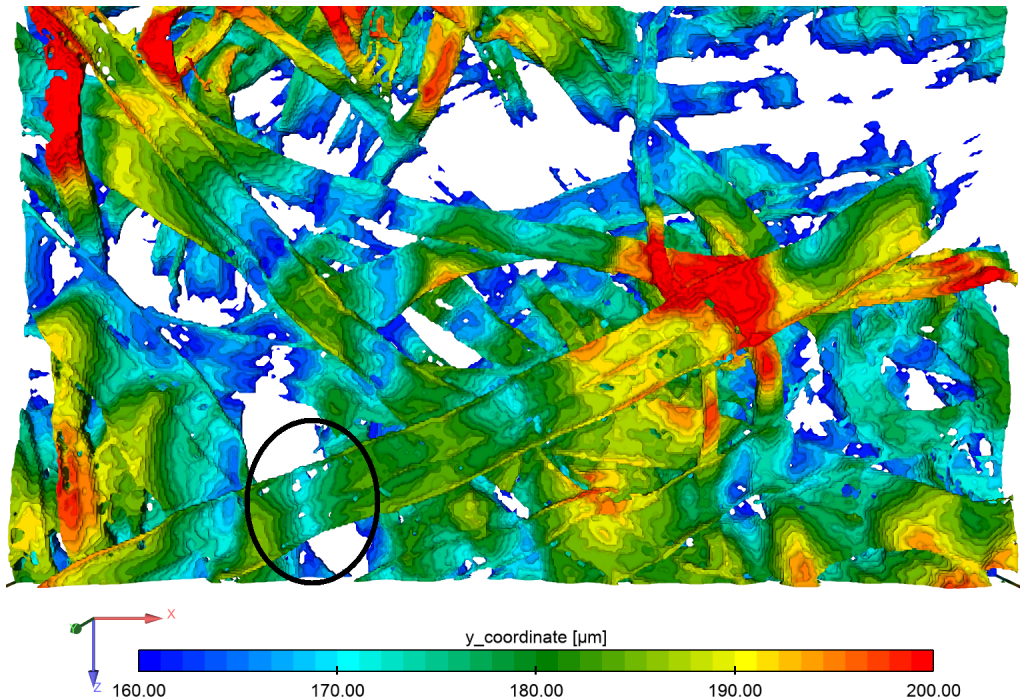


Figure 3.13: S₃ R₁ 5 x scaled segmentation

3.4.4 Conclusion of the Segmentation Methods

The conclusion of the visual inspection of the different segmentation methods is that the 5 x scaled segmentation closes the most holes in the fibres, but there are still holes which might not be realistic. For further studies it might be helpful to have scanning electron microscope images of exactly the same paper web which is afterwards used for μ -CT. This would allow for a more detailed geometry comparison of the virtual model with the sample and there, a further improvement of the segmentation method.

4 Mesh Creation

Many different commercial software tools are available for 3D mesh creation. Some of these tools are used in CT and μ -CT studies, especially for medical and material science applications. Some of this challenging work can be found in [Bay14], [Miy13] and [E13]. Having such a complex geometry like paper and meshing the air volume between fibres, special tools have to be used. In the present case the mesh length scale has to be smaller than $1.5\mu\text{m}$ to utilize the voxel size of the μ -CT data. Furthermore, all pores are required to model the air flow through the paper web properly. Making a simple forecast to evaluate mesh size it is useful to estimate the amount of nodes. The number of nodes n is the sample length divided by r which is the smallest length scale in the mesh in μm . For a volume Equation 4.1 can be used to make a rough estimate for the amount of nodes to describe the volume.

$$n = \frac{\text{length}}{r} \cdot \frac{\text{width}}{r} \cdot \frac{\text{height}}{r} \quad (4.1)$$

Table 4.1 gives the solution of Equation 4.1 for different segment sizes and different mesh length scales to describe the volume. The results show that a simulation with the required amount of nodes to resolve the full paper web sample with $0.5\mu\text{m}$ is not possible (full sample). The upper limit for the smallest length scale in the mesh is the voxel length which is $1.5\mu\text{m}$.

A flow field in a mesh with $2 \cdot 10^7$ nodes can be solved, with an CFD software installed on a workstation with 132GB RAM. Cutting the volume into 12 segments reduces the required nodes by the same factor, but this is still not enough (1/12 segment). This is the reason for using a meshing trick, the fibre material is very anisotropic, so a high resolution is required representing the thickness of the paper web (for example to resolve the

4 Mesh Creation

gap between 2 fibres). That was the reason for scaling the geometry by a factor of 2 in the thickness direction. This allows for the meshing program to resolve gaps between fibres with a good accuracy and an acceptable amount of nodes (1/12 segment scaled). The estimation gives a good forecast in this study, since the size of the mesh elements will not change much in our volume. Solving other problems many nodes can be saved increasing the mesh element size with the distance from the smallest gap.

Table 4.1: Estimation Mesh Size

name of the sample	sample size [μm]	length scale [μm]	nodes
full sample	2812.5 x 2000.5 x 166.5	0.5	$7.50 \cdot 10^9$
1/12 segment	700.5 x 667.5 x 166.5	0.5	$6.23 \cdot 10^8$
1/12 segment scaled	700.5 x 667.5 x 333	1.5	$4.61 \cdot 10^7$

Table 4.1 shows that a mesh of the "full sample" would contain far too many nodes for a simulation, splitting the mesh into 12 segments would reduce the amount of nodes but not enough to make a simulation possible. An increase of the smallest mesh element is required to create a mesh which allows a simulation on a workstation. The expected mesh size is $5 \cdot 10^7$.

4.1 Basis mesh

Figure 4.2 gives some details of the meshing process. The two times scaled geometry can be seen in 4.2_a and 4.2_b shows the according mesh. Figure 4.3 shows the original dimensions. All small gaps between the fibres are resolved using this scaling method. Pores without connection to the outer air are not meshed. HEXPRESS/Hybrid [num19] is the meshing software to solve this task. The mesh starts in a seeding point in the air volume if pores are not connected to the seeding point the mesh solver can not reach them and they are not taken into account. Some examples of the used 3D elements which are placed in the volume can be seen in Figure 4.1.

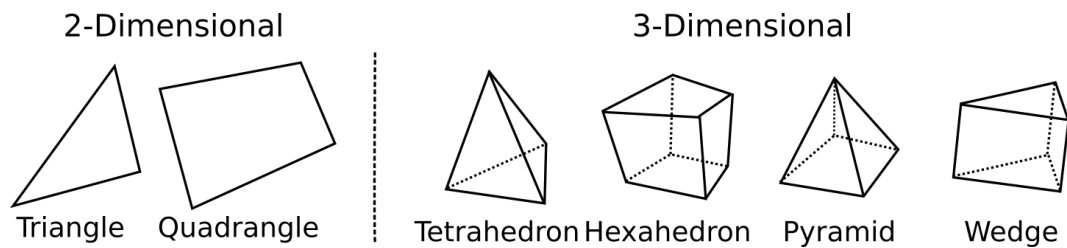


Figure 4.1: Volume elements used for creating CFD meshes

4 Mesh Creation

Comparing 4.2_a and 4.2_b, it can be clearly seen that lots of the pores are not connected to the outer air. The red rings show zones of the geometry which are connected to the air, the black ring shows details of the geometry which are not connected to the outer air. The meshing program works with a seed point. Starting from this point the program meshes all regions of the geometry which can be reached from the starting point.

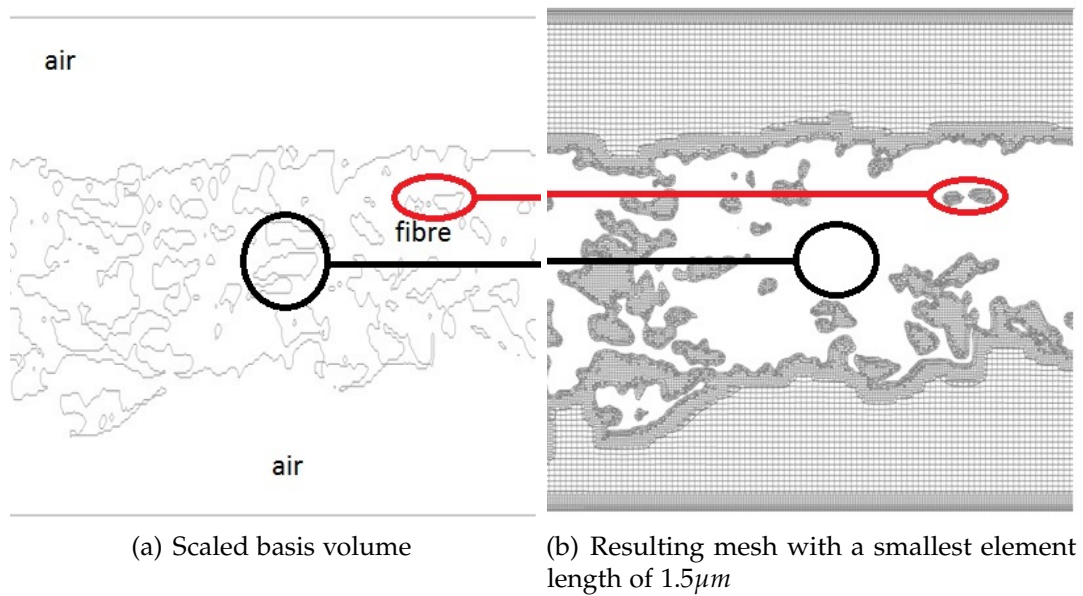


Figure 4.2: Scaled and meshed geometry

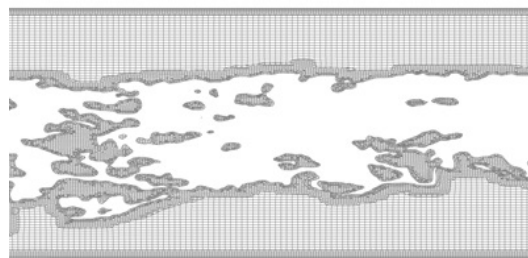


Figure 4.3: Mesh in original size of the μ -CT scan resolving all gaps between fibres

The final meshes contain about $1.3 \cdot 10^7$ to $1.8 \cdot 10^7$ nodes. Half of the nodes estimated can be spared since the fibre material contains no nodes and the

4 Mesh Creation

mesh size was increased by a factor of 2 in a distance of 5 cells from the fibre surface.

Figure 4.4 shows some details of the final basis mesh. The meshed fibre material surface is coloured with the y-coordinate, it is clearly visible that two cells describe one voxel height. This is the reason for the stair step look.

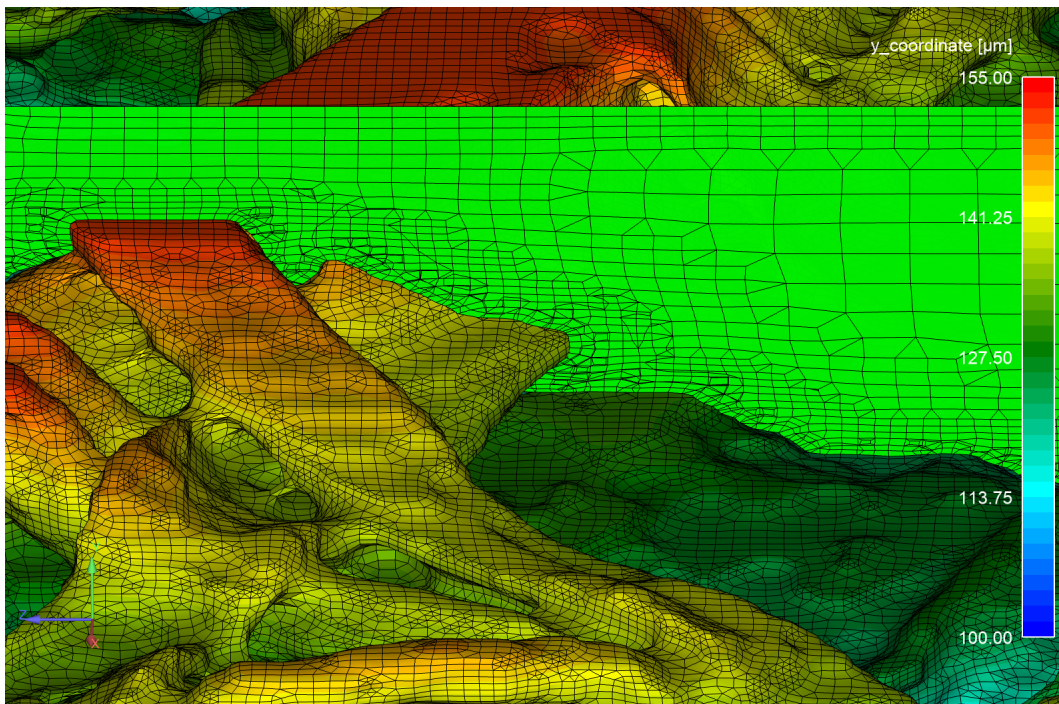


Figure 4.4: Basis mesh in original size

4.2 Double resolution mesh

To prove that the basis mesh is accurate, three of the segments have been meshed with half the element size of the basis mesh. That means that the double resolution mesh contains eight times more nodes than the basis mesh. To run a simulation a normal workstation is not enough, about 500GB RAM are required to load and run such a big mesh. One segment contains about 115 millions nodes.

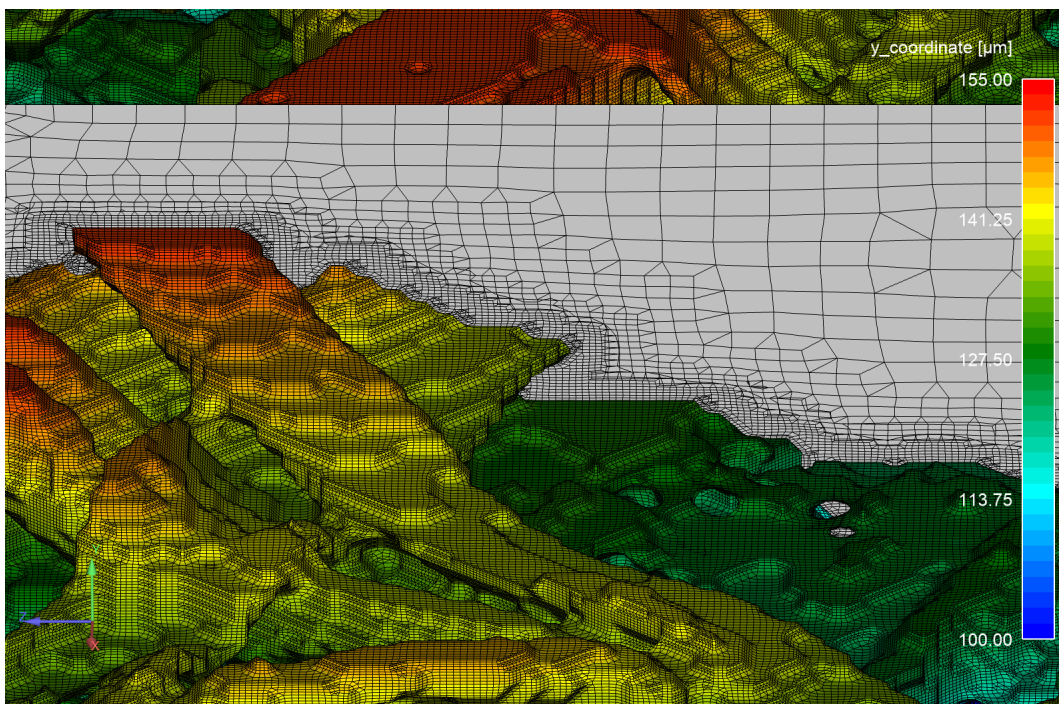


Figure 4.5: Eight times finer mesh

Figure 4.5 shows a detail of the eight times finer mesh. The meshed fibre material surface is coloured with the y-coordinate. Now four elements describe the height of one voxel. The mesh is eight times bigger since the smallest length of the basis mesh was reduced by half. The example of a cube explains well the increase of required nodes in the mesh. Using a cube with a length of 1, each side of the cube is now split into half, the result is an amount of eight cubes. The same happens with the mesh if the

4 Mesh Creation

smallest mesh size is divided by a factor of two, the mesh will be eight times bigger.

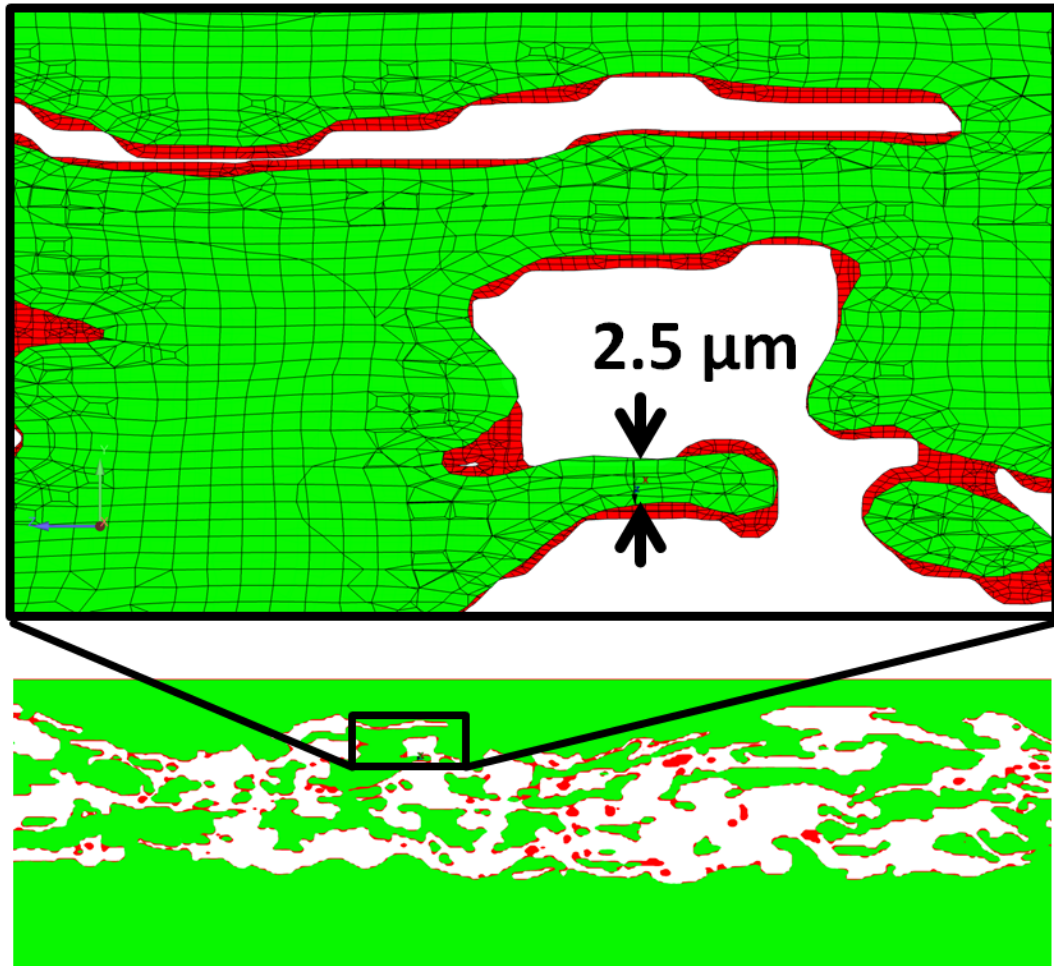


Figure 4.6: Four times finer mesh

Figure 4.6 give a visual comparison of the two different meshes used for the mesh study (basis and double resolution mesh). The green surface is a clip plane of the basis mesh, the red surface is exactly the same clip plane produced with the double resolution mesh. The image demonstrates that the smaller length scale of the double resolution mesh allows the meshing program to enter more pores in the geometry. All red surfaces in the image

4 Mesh Creation

are zones which are a result of the meshing process using the smaller length scale. The detail shows the differences of the two meshes. The arrows mark a distance of $2.5\mu m$. The smaller length scale of the double resolution mesh also shows more details in this comparison. If unlimited hard and software resources would be available the meshing process with the smaller length scale should be chosen just to secure a proper geometry description.

The result of the flow field is compared in chapter 6, it demonstrates that the influence of the segmentation is much bigger than the influence of mesh. To generate accurate results of the flow field through the paper web a proper description of the geometry is required and this is fulfilled by using the basis mesh method.

5 Solver and Boundary Conditions

5.1 Computational Fluid Dynamics CFD

5.1.1 Basic Equations of Fluid Mechanics

In this work only laminar flow can be expected as demonstrated in section 5.2. Solving laminar flows is less complex than turbulent flow problems, since the turbulence of the fluid needs not to be taken into account. The energy equation is required because the air is modelled as ideal gas. This is required to simulate the process boundary condition (section 5.3) in which compressibility effects have to be modelled. Following equations have to be solved in the flow situation [Hel16]:

Time dependent and compressible Navier Stokes Equations:

$$\frac{\partial \rho}{\partial t} + \nabla \cdot (\rho \mathbf{u}) = 0 \quad (5.1)$$

$$\frac{\partial(\rho \mathbf{u})}{\partial t} + \nabla \cdot (\rho \mathbf{u} \mathbf{u}) + \nabla p = \rho \mathbf{f} + \nabla \cdot \boldsymbol{\tau} \quad (5.2)$$

$$\frac{\partial e}{\partial t} + \nabla \cdot [\mathbf{u} \cdot (e + p)] = \frac{\partial Q}{\partial t} + \rho \mathbf{f} \cdot \mathbf{u} - \nabla \cdot \mathbf{q} + \nabla \cdot (\boldsymbol{\tau} \cdot \mathbf{u}) \quad (5.3)$$

5 Solver and Boundary Conditions

Inner total energy:

$$e = \frac{p}{\kappa - 1} + \rho \frac{\mathbf{u} \cdot \mathbf{u}}{2} \quad (5.4)$$

Heat conduction:

$$\mathbf{q} = -k \cdot \nabla T \quad (5.5)$$

Equation 5.1 is the equation of mass conservation, Equation 5.2 is the momentum equation and Equation 5.3 is the equation of energy conservation.

Equation 5.4 is the equation of inner total energy. Equation 5.5 is the equation of the heat conductivity.

In the equations ρ is the density in $[kg/m^3]$, t is the time in $[s]$, ∇ is the gradient of a function or a vector in $[1/m]$, \mathbf{u} is the velocity vector in $[m/s]$, $\boldsymbol{\tau}$ is the strain tensor in $[kg/ms^2]$, f is the bodyforce (e.g. the gravity) in $[m/s^2]$, e is the inner total energy in $[kg/ms^2]$, \mathbf{q} is the heat conduction in $[W/m^2]$ and Q is an internal heat source in $[J/m^3]$. κ is the isentropic coefficient and p the static pressure in $[Pa]$. k is the heat conductivity coefficient in $[W/mK]$ and T the static temperature in $[K]$.

Simplified Navier Stokes Equations (stationary and compressible):

$$\nabla \cdot (\rho \mathbf{u}) = 0 \quad (5.6)$$

$$\nabla \cdot (\rho \mathbf{u} \mathbf{u}) + \nabla p = \nabla \cdot \boldsymbol{\tau} \quad (5.7)$$

$$\nabla \cdot [\mathbf{u} \cdot (e + p)] = \nabla \cdot (\boldsymbol{\tau} \cdot \mathbf{u}) \quad (5.8)$$

For these simulations the equations can be simplified to the stationary or timely independent form, details how the equations are solved in the CFD solver can be found in [ANS13]. Equation 5.6 is the stationary continuity equation which says that masses can neither disappear nor be generated without sinks or sources. Mass can only be transported over the system boundary.

5 Solver and Boundary Conditions

The first term of the momentum equation which can be seen in Equation 5.7 describes the convective term, which stands for the momentum flow. The change in the momentum caused by pressure is determined in the second term. The third term describes viscous shear forces.

Equation 5.8 shows the stationary compressible energy equation. Similar to the previous equations, the left term describes the energy flux across the system boundary. The term on the right describes the energy change based dissipation or internal friction.

5.1.2 Discretization

A continuous volume in which the flow is to be investigated, is replaced by a set of discrete points, represented by a "grid" or "mesh", which is built up by sub-volumes containing elements like Figure 4.1. In the mesh the points are distributed arbitrarily in the volume. Every point is connected with its neighbour points, so that the resulting surface pieces usually have triangular or hexa shapes. The relationship between nodes and elements is determined by an assignment matrix. In the sub-volumes the numeric equations can be solved. The fluxes of mass Equation 5.1, of momentum Equation 5.2 and energy Equation 5.3 are solved in each volume using different numerical codes until balance is achieved.

5.1.3 Finite-Volume Methods (FVM)

The total volume is directly discretized in physical space by splitting the domain into finite volumes or cells Figure 4.1. These come in the form of general bodies with four, five or six side surfaces (tetrahedron, prism, hexahedron or polyhedra). First, the basic equations over the volume Equation 5.1, Equation 5.2 and Equation 5.3 of the whole integration area are integrated. The surface integral can therefore be summed over the side surfaces of a volume cell. For every single volume cell the basic equations are approximated. Discretization is done at the cell midpoint. The flux entering a given volume is identical to that leaving the adjacent volume if there are no sources or sinks (conservation of the flow variables). This is the

5 Solver and Boundary Conditions

main advantage of finite volume methods as opposed to other discretization methods.

5.2 Gurley Boundary Conditions

The boundary conditions for the CFD simulation have to be equivalent to the Gurley measurement. The Gurley measures the time of $100ml$ air pressed through the paper with an area of $6.452cm^2$ at $1.22kPa$ pressure drop. In the CFD simulation the pressure drop is set. The volume flow is a result of the simulation. The used air temperature is $25^\circ C$. The air was modelled with the ideal gas law. For the simulations the commercial software ANSYS Fluent V15 is used. The solver is pressure based coupled in double precision [ANS13]. The viscosity is modelled laminar ($\nu = 1.838 \cdot 10^5 Pas$). The density is a function of pressure and temperature. The operating pressure is set to one atm ($101325Pa$). The inlet is modelled as pressure inlet with a relative pressure of $1220Pa$, the outlet is a pressure outlet with $0Pa$. Figure 5.1 gives an overview of the boundary conditions are set and how the air is flowing through the paper driven by the pressure difference.

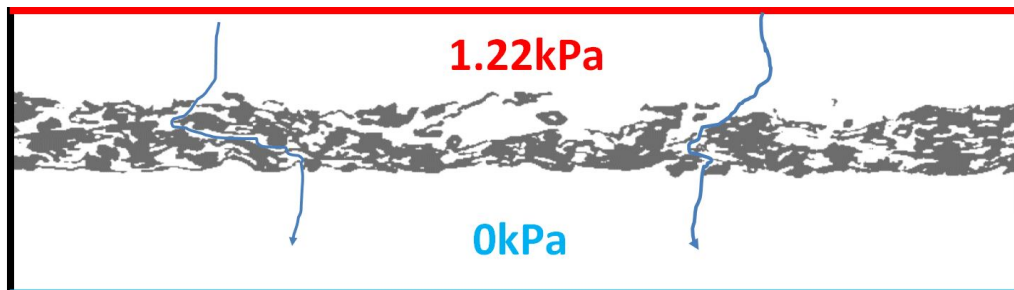


Figure 5.1: Sketch of the boundary conditions for the Gurley measurement

5.3 Process Boundary Conditions

In another investigation the process boundary conditions have been investigated. In the industrial process the paper bags are filled with cement, flour or other powders. This process operates with a much bigger pressure difference than the Gurley measurement. One goal of the work is to identify differences of the flow field due to a change in the boundary conditions. The pressure drop in the process condition is 5[bar].

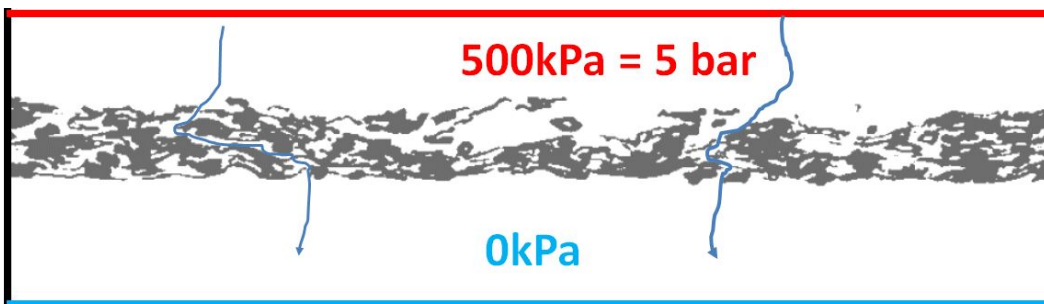


Figure 5.2: Sketch of the boundary conditions, for industrial filling of the sacks

5.4 Analytical Estimations

Before a CFD simulation is started, it is always useful to check a couple of dimensionless numbers. This helps to evaluate the expected flow field. In this work the Reynolds number is important due to the fact that the flow field is modelled laminar. In pipes the Reynolds number is lower than 2300 for laminar flow. In the paper web there are no "pipes" but the pores are assumed to be "micro channels" with a typical diameter and an according average velocity. Having an diameter d , a average velocity v_{av} which is assumed to be 5[m/s] (based on simulation results) and the kinematic viscosity ν in [m²/s], the Reynolds number can be calculated as follows:

$$Re = \frac{v_{av} \cdot d}{\nu} \quad (5.9)$$

5 Solver and Boundary Conditions

Table 5.1: Estimation Reynolds number for Gurley boundary conditions

d [μm]	v_{av} [m/s]	ν [m^2/s]	Re [-]
2	5	1.56e-05	0.64
40	5	1.56e-05	12.84
100	5	1.56e-05	32.05

The diameters d are chosen for a wide range, $2\mu m$ is the lower limit coming from the smallest length scale of the mesh, $40\mu m$ is a big pore and $100\mu m$ is roughly the thickness of the paper web. The results in Table 5.1 show that for Gurley boundary conditions, the Reynolds number is by far too small for turbulent flow conditions.

Table 5.2 gives the same estimation for the process boundary condition (5[bar] pressure drop). The average velocity v_{av} is now estimated to be $400[m/s]$ in the micro channels, which is faster than the speed of sound. The speed of sound is roughly an upper limit for the flow velocity having super critical conditions.

Table 5.2: Estimation Reynolds number for process boundary conditions

d [μm]	v_{av} [m/s]	ν [m^2/s]	Re [-]
4	400	1.56E-05	125.35
40	400	1.56E-05	1253.53
100	400	1.56E-05	2564.10

The estimation result shows that it is required to have a channel diameter d of at least $100[\mu m]$ and an average velocity v_{av} of $400[m/s]$ to reach a Reynolds number Re slightly bigger than the critical Reynolds number of 2300. Since these analytical equations work only in a fully developed flow regime with a long enough inlet section, we can be sure to have laminar conditions. The application of the laminar model for the CFD simulation, based this estimation is valid.

Using 5 bar pressure difference has a massive impact on the flow, which is now to be expected a critical flow. That means the Mach number is now bigger than 1. Equation 5.9 gives a definition of the Mach Number for ideal

5 Solver and Boundary Conditions

gases. If the Mach number is bigger than one, the flow is super sonic. In Equation 5.9, v is the local velocity in $[m/s]$, a is the speed of sound in $[m/s]$, κ is the isentropic exponent which has a value fo 1.4[-] for air, R is the specific gas constant for air which has a value of 287.1 $[J/kgK]$ and T is the temperature in $[K]$.

$$Ma = \frac{v}{a} = \frac{v}{\sqrt{\kappa \cdot R \cdot T}} \quad (5.10)$$

Table 5.3 gives an estimation for the Mach number at Gurley and process boundary condition (5 bar pressure drop). Resulting velocities bigger than the speed of sound have to be expected.

Table 5.3: Estimation Mach number for different boundary conditions

Boundary conditions	v_{av} $[m/s]$	a $[m/s]$	Ma [-]
Gurley	5	346.12	0.014
Process	400	346.12	1.156

The modelling for Gurley conditions was prepared such a way that only the pressure in the inlet needs to be changed for switching to process boundary conditions. This ensures a good comparability between the results, which are supposed to show the pure influence of the pressure change on the flow field.

All physical variables are defined, the following sections focus on the results. We are starting with the influence of the segmentation and the influence of the mesh resolution. Next, we focus on the comparison of the result of the basis segmentation and the 5 x scaled result. In the final evaluations the focus is on the porosity and the flow through the pores and how it is distributed over the individual pores.

6 Effect of Segmentation Method and Mesh Resolution

6.1 Effect of Segmentation

The following section shows the result of one segment (*S3R1* see Figure 3.8). The used image set is generated using different segmentation methods. Three different results are compared. Goal is the evaluation of the segmentation method and its influence on the resulting fibre web and finally the flow rate. Details of the different segmentation methods can be found in chapter 3 and in [Mac18].

Figure 6.1 on the left shows the resulting geometry. The stair steps are a result of the geometry build up based on the image set. On the right in the CFD result, the same holes can be detected. These holes are not realistic in fibres, so they are probably a result of the segmentation.

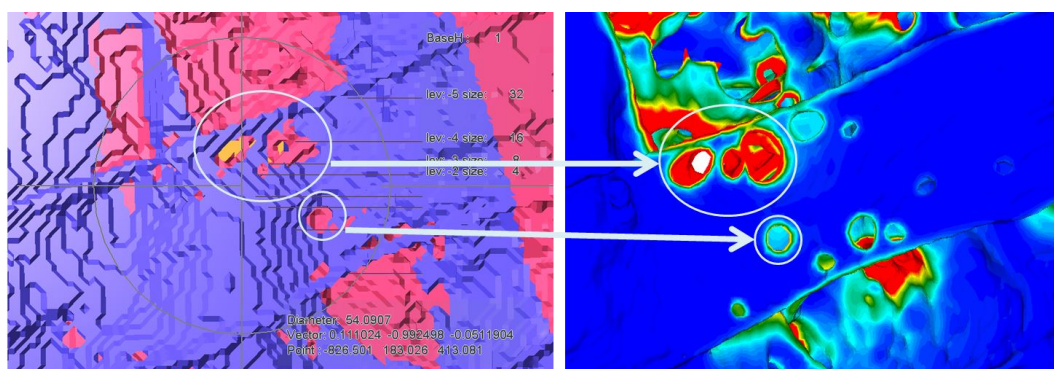


Figure 6.1: Resulting geometry (left) and CFD result (right) in detail, showing some holes

6 Effect of Segmentation Method and Mesh Resolution

To investigate those holes in the fibres more in detail three different image sets are produced. The difference is only the segmentation method. Figure 6.2, Figure 6.3 and Figure 6.4 show the post processed CFD results on the fibre web. The colour plotted corresponds to the wall shear in Pa. This value is useful for hole detection, high wall shear shows regions in which the air has a high velocity near the wall.

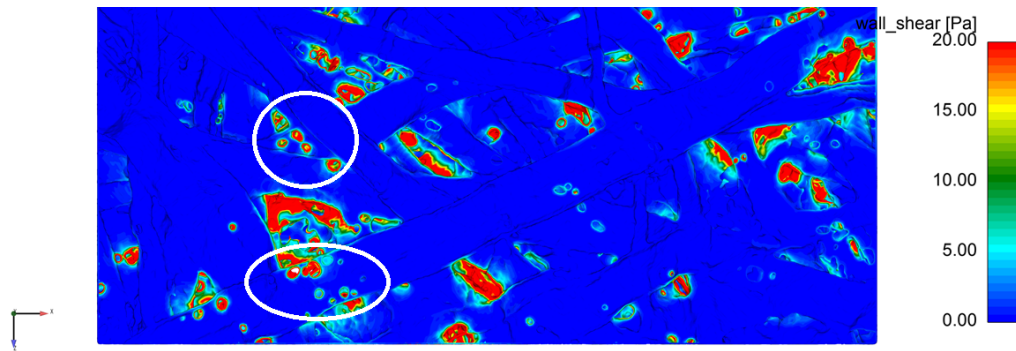


Figure 6.2: Basis segmentation, showing many holes

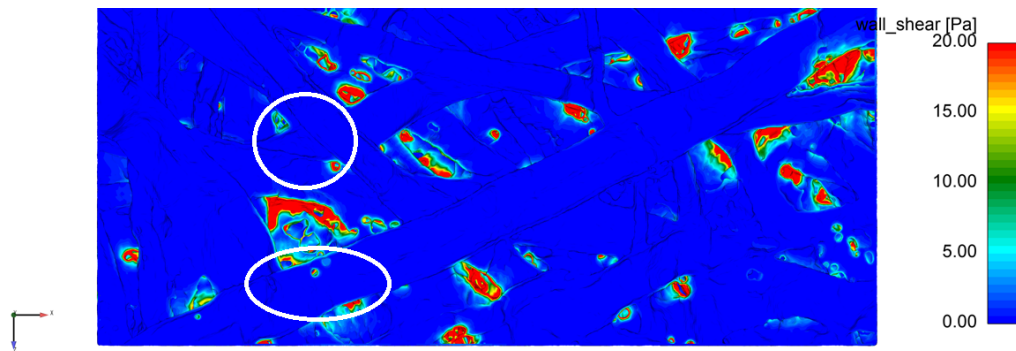


Figure 6.3: 3 x scaled segmentation, showing some holes

6 Effect of Segmentation Method and Mesh Resolution

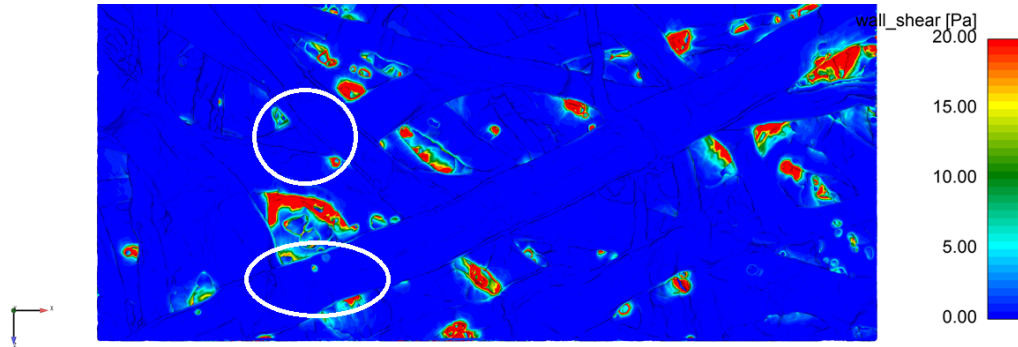


Figure 6.4: 5 x scaled segmentation, showing less holes

$$\tau_w = \mu \cdot \left. \frac{\partial v}{\partial y} \right|_{y=0} \quad (6.1)$$

Equation 6.1 gives the definition of the wall shear, τ_w is the wall shear in $[Pa]$, v is the velocity of the fluid in $[m/s]$, y is the coordinate normal to the wall in $[m]$ and μ is the dynamic viscosity in $[Pas]$. The bigger the gradient on the wall the bigger the resulting wall shear.

Table 6.2 shows the results in detail. All of the CFD simulation results of this segment *S1R3* are bigger than the measured average. However, looking into the pictures Figure 6.2, Figure 6.3 and Figure 6.4 the 5 x scaled segmentation result seems to be the most proper one because it is the geometry with the smallest amount of holes in the fibres. The holes can be seen in the images in red colour. A comparison of the flow rate shows that the 5 x scaled is the closest to the measurement, this is also the result which indicates less fibre holes than the others. For the final results the 5 x scaled segmentation process is used.

6 Effect of Segmentation Method and Mesh Resolution

Table 6.1: Results of different segmentation methods in comparison to the measurement

name of the result	Gurley time [sec]	velocity [m/s]	times the measurement
Gurley measurement	6.82	0.0227	1
CFD basis segmentation	1.070	0.1448	6.37
CFD 3 x scaled segmentation	1.648	0.0940	4.14
CFD 5 x scaled segmentation	1.810	0.0856	3.7671

6.2 Influence of the Mesh Resolution on the Flow Rate

Table 6.1 shows that the segmentation has a huge influence on the flow rate, the basis segmentation has nearly double the flow rate as the 5 x scaled segmentation. Now the basis segmentation of three different segments is used for a meshing study. Goal is to figure out the influence of the smallest mesh length scale on the flow rate. The segments which have been used are *S1R1*, *S2R3* and *S4R1*. The smallest length scale of the mesh elements for a description of the paper web geometry is reduced in this study from $1.5\mu m$ to $0.75\mu m$ (further details in chapter 4).

Using an eight times bigger mesh (8 times more nodes) has a small influence on the result in comparison to the segmentation. The 5 x scaled segmentation has nearly half the flow rate than the basis segmentation. The eight times bigger mesh has a flow rate which is about 10% bigger than the basis. Since the extra fine mesh containing more than 110 million nodes and requiring 550 GB RAM on a cluster changes the result in a much smaller way than the segmentation, all further results are calculated using the basis mesh setup, see section 4.1.

6 Effect of Segmentation Method and Mesh Resolution

Table 6.2: Results of different meshing methods for the basis segmentation

name of the result	Gurley time [sec]	velocity [m/s]	times the measurement
Gurley measurement	6.82	0.0227	1
CFD basis segmentation S ₁ R ₁	1.0569	0.1466	6.45
CFD basis segmentation S ₁ R ₁ eight times more nodes	0.924	0.168	7.37
CFD basis segmentation S ₂ R ₃	2.1564	0.079	3.61
CFD basis segmentation S ₂ R ₃ eight times more nodes	1.829	0.0847	3.72
CFD basis segmentation S ₄ R ₁	0.583	0.266	11.69
CFD basis segmentation S ₄ R ₁ eight times more nodes	0.5361	0.289	12.72

7 Results of the total Sample (3 x 4 Segments)

7.1 Basis Segmentation Results

For the first set of simulations the basis segmentation process is used (chapter 3). All 12 segments are processed in the exact same way. The geometry generation, the meshing process (section 4.1) and the boundary conditions (chapter 5) were performed in exactly the same way. Table 7.1 shows the results in detail. The modelled average flow velocity of the 12 segments is 7.0 times the measured flow rate. The maximum value of the CFD result is 11.69 times the measured flow rate, the minimal value is 3.16 times the measured flow rate. Figure 7.1 shows the distribution of the flow rate. Depending on the position of the segment the local flow rate is different. The right figure visualizes the distribution, the left figure shows the 12 segments with the according average velocity. In conclusion, the resulting velocity modelled from the basis segmentation is much larger than the velocity of the measurement.

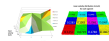


Figure 7.1: CFD Result of all 12 segments using the basis segmentation

7 Results of the total Sample (3 x 4 Segments)

Table 7.1: Basis segmentation simulation results sack kraft paper

Section	Gurley time [s]	velocity [m/s]	times the measurement
S1 R1	1.0569	0.1466	6.4528
S1 R2	0.6788	0.2283	10.0479
S1 R3	1.2329	0.1257	5.5315
S2 R1	0.9193	0.1686	7.4185
S2 R2	1.4311	0.1083	4.7656
S2 R3	2.1564	0.0719	3.1626
S3 R1	1.0701	0.1448	6.3734
S3 R2	0.7727	0.2006	8.8267
S3 R3	0.8905	0.1740	7.6584
S4 R1	0.5832	0.2658	11.6949
S4 R2	1.5702	0.0987	4.3435
S4 R3	0.8302	0.1867	8.2152
AV	0.9686	0.1600	7.0409
Min	2.1564	0.0719	3.1626
Max	0.5832	0.2658	11.6949

7.2 5 x Scaled Segmentation Results

Then, the 5 x segmentation process was applied (section 3.3). All 12 segments are processed in the exact same way as in the previous chapter. The average of the modelled air flow of the 12 segments is 4.2 times the measured flow. The maximum value of the CFD result is 7.16 times the measured flow, the minimal value is 1.88 times the measured flow. Table 7.2 shows the results in detail.

Figure 7.2 shows the distribution of the flow rate. Depending on the position of the segment, the local flow rate again is different. The right figure visualizes the distribution, the left figure shows the 12 segments with the according average velocity. In comparison to the basis segmentation, the CFD simulations of the 5 x scaled segmentation method are closer to the measured values. The flow rate through the sample is smaller because the holes in the fibres are closed.

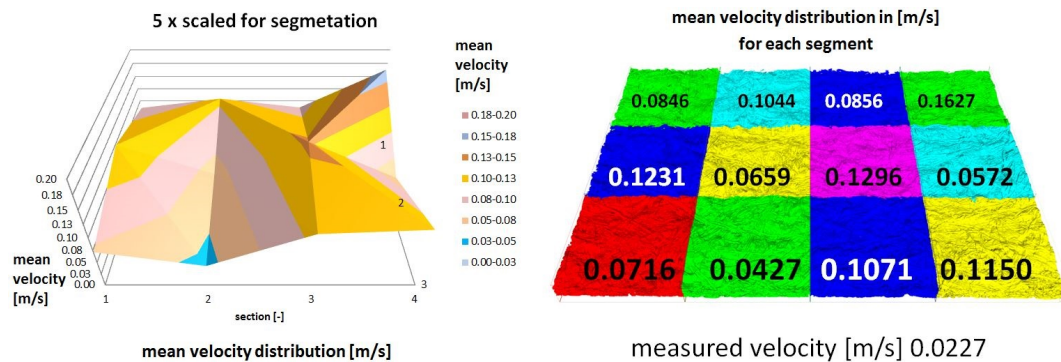


Figure 7.2: CFD Result of all 12 segments using the 5 x scaling method

7 Results of the total Sample (3 x 4 Segments)

Still, the average flow rate of the CFD simulation is four times higher than the measured flow rate. Not even the flow rate of the segment with the minimum flow is smaller than the measured flow rate. These facts and the holes in the fibres (Figure 3.13) show that the segmentation should be further optimized. The most challenging problem is for sure the huge amount of data that has to be managed and thereof resulting large geometry files. A visual inspection can also help in further investigations using the thickness coordinate (y-coordinate in this work) for hole detection. A visual comparison of SEM images and the geometry created with any segmentation method can also help to improve the quality of further CFD simulation results, due to the fact that the uncertainty of differences between the geometry modelled in CFD and the real geometry can be reduced.

Table 7.2: 5 x scaled segmentation simulation results sack kraft paper

Section	Gurley time [s]	velocity [m/s]	times the measurement
S1 R1	1.8331	0.0846	3.7205
S1 R2	1.2588	0.1231	5.4177
S1 R3	2.1630	0.0717	3.1531
S2 R1	1.4851	0.1044	4.5923
S2 R2	2.3535	0.0659	2.8978
S2 R3	3.6249	0.0428	1.8814
S3 R1	1.8104	0.0856	3.7671
S3 R2	1.1957	0.1296	5.7036
S3 R3	1.4469	0.1071	4.7134
S4 R1	0.9525	0.1627	7.1604
S4 R2	2.7083	0.0572	2.5182
S4 R3	1.3471	0.1151	5.0629
AV	1.6178	0.0958	4.2157
Min	3.6249	0.0428	1.8814
Max	0.9525	0.1627	7.1604

7.3 5 x Scaled Segmentation Results at Process Boundary Conditions (5bar)

Now the 5 x segmentation is also used to calculate the flow rates at process boundary conditions. Now, compressibility effects are important. Since the pressure difference is super critical, Mach numbers higher than one can be expected Equation 5.9. The details can be seen in Table 7.3. The average velocity is now more than 100 times higher than in the Gurley boundary conditions.

Table 7.3: 5 x scaled segmentation simulation results sack kraft paper

Section	times the basis result	velocity [m/s]	normalized flow rate
S1 R1	182.729	15.450	0.992
S1 R2	161.112	19.837	1.274
S1 R3	186.029	13.330	0.856
S2 R1	151.326	15.793	1.014
S2 R2	183.847	12.107	0.777
S2 R3	187.885	8.033	0.516
S3 R1	168.477	14.424	0.926
S3 R2	148.825	19.291	1.239
S3 R3	148.122	15.866	1.019
S4 R1	137.391	22.357	1.436
S4 R2	203.977	11.673	0.750
S4 R3	162.729	18.723	1.202
AV	169.0654	15.2874	0.9816
Min	137.3906	8.0335	0.5158
Max	203.9774	22.3570	1.4356

7 Results of the total Sample (3 x 4 Segments)

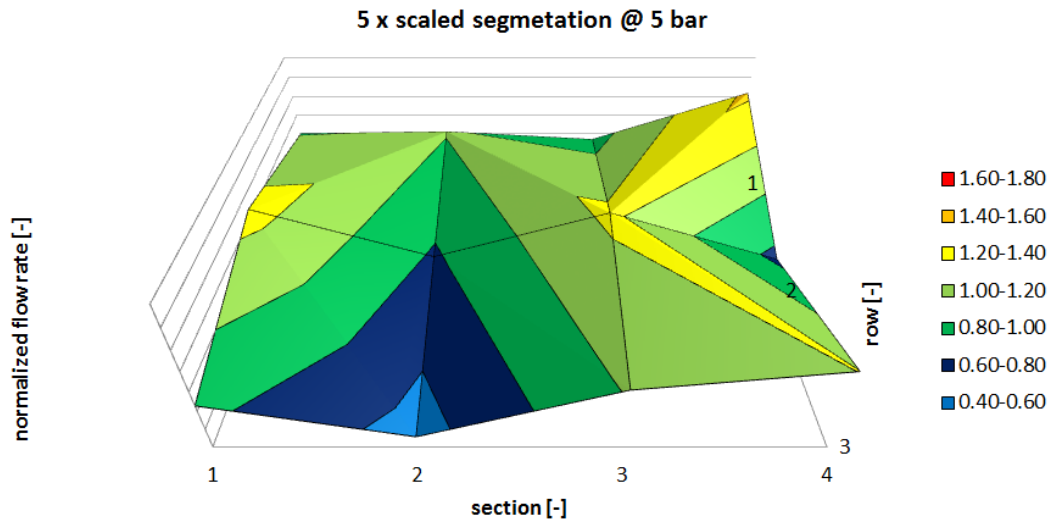


Figure 7.3: CFD Result of all 12 segments using the 5 x scaling method at 5 bar pressure difference

Figure 7.3 shows the distribution of the flow rate. Depending on the position of the segment the local flow rate is different. A comparison with the Gurly boundary conditions shows that now the differences between the single segments are a bit smaller but show the same tendency as the simulation results with the Gurley boundary conditions. A reason for the flattening process is the high Ma number which limits the velocity in the paper web pores to $Ma = 1$. To generate higher Ma numbers Laval geometries are required.

7.4 Comparison of the Segmentation Methods

Now the results of the different segmentation methods are compared. The most interesting question to answer is how the flow changes with the segmentation method. A comparison of the flow rates can be done by comparing Figure 7.4 and Figure 7.5. Both diagrams show the normalized flow rate. The deviation of the single segment flows from the average flow is very similar for both methods.

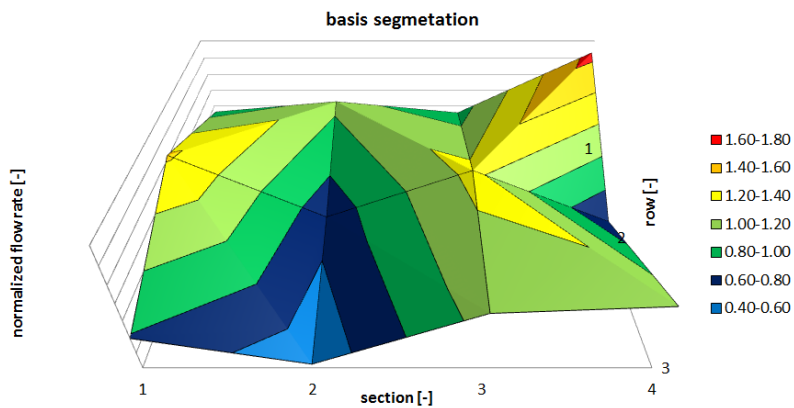


Figure 7.4: Basis scaling method, normalized flow rate

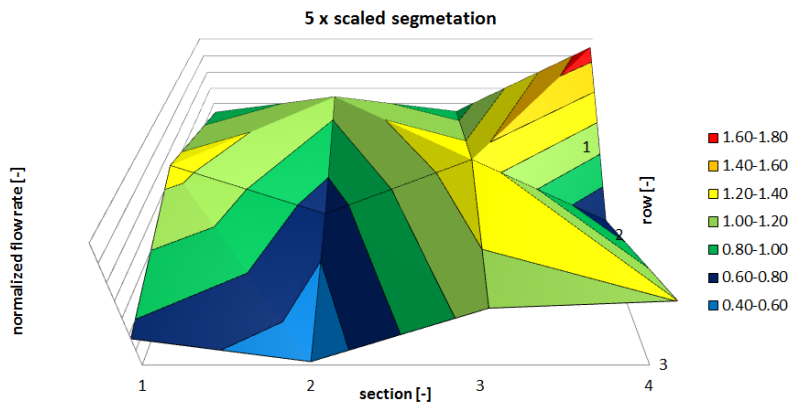


Figure 7.5: 5 x scaling method, normalized flow rate

7 Results of the total Sample (3 x 4 Segments)

Figure 7.6 shows the difference between the two segmentation results in percent. There is no clear tendency, but the deviation between the normalized flow rates is not bigger than 10%. As a reminder, the result of the basis segmentation flow rate is about 7 times, the 5 x scaled segmentation flow rate is 4 times higher than the measured flow rate with the Gurley method. This big difference does not really change the local deviation of the single sections.

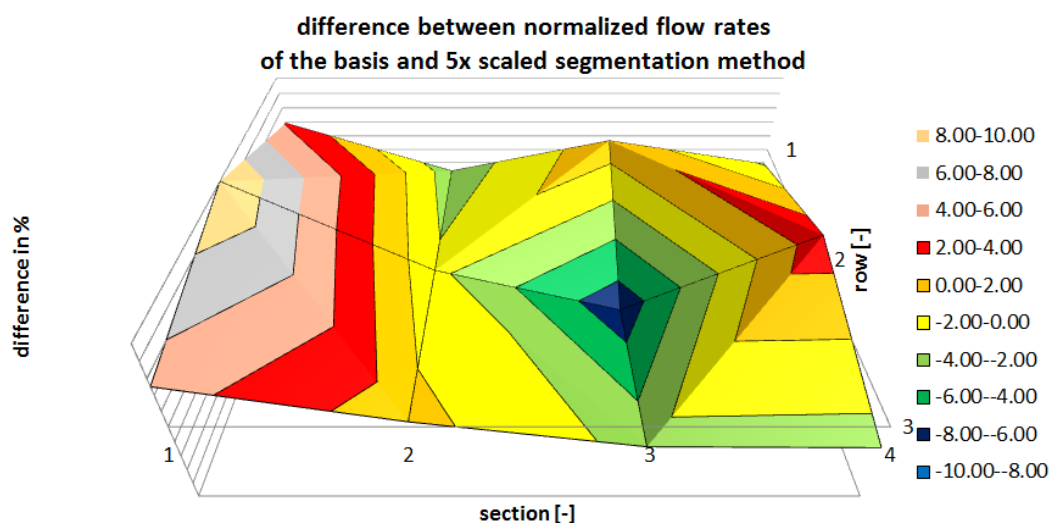


Figure 7.6: Difference between normalized flow rates in percent

The conclusion of the comparison is that the 5 x scaled segmentation homogeneously reduces the permeability of the data set. The fact that the 5 x scaled segmentation closes holes in the fibres has been documented in chapter 3, it seems that the unrealistic holes are also homogeneously closed in the inner zones of the geometry of the paper web. The segmentation does not effect the local variances of the permeability, only the global permeability gets smaller.

7.5 Comparison of the Measurement Results and the 5 x Scaled Segmentation Result

Finally, a comparison of the measurement and the 5 x scaled segmentation result can be seen in Figure 7.7. Since the paper has inhomogeneous structures much larger than the sample size, more samples would be required to get better statistics. Still, the result is close to the measured value. The Gurley uses an area of about 654.2mm^2 , the total sample was $2.8\text{mm} \times 2\text{mm}$ the single sections have areas of 0.4676mm^2 . The best fitting section is S2R3 which can be found in the middle of the diagram Figure 7.7. The diagram shows a comparison of the result based on the average velocity of each segment, with the average velocity based on the Gurley measurement. The section S4R1 has the largest deviation from the measured values. The maximum and the minimum value of the Gurley measurement are shown in the diagram as reference.

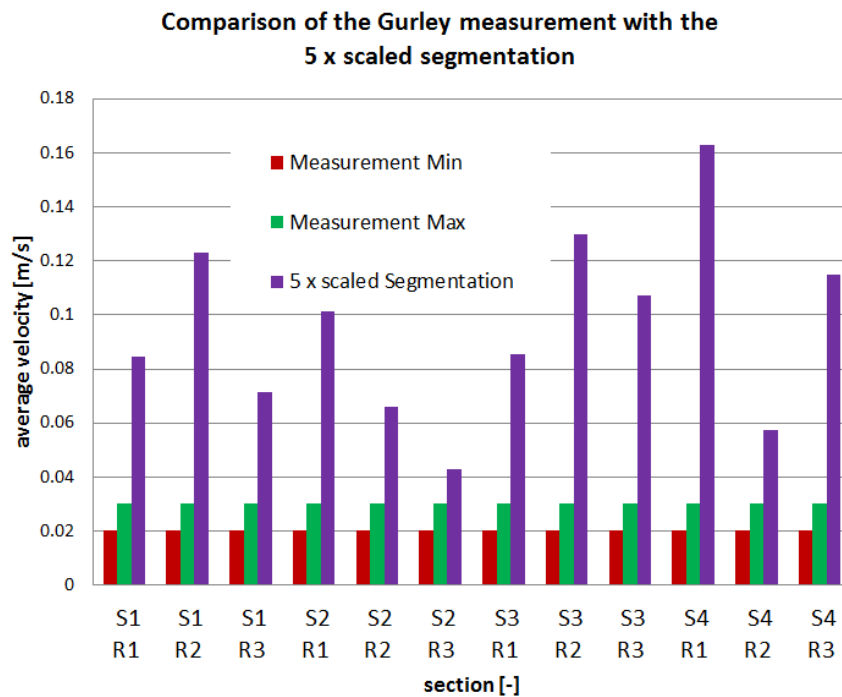


Figure 7.7: Comparison measurement vs. CFD

8 Porosity

8.1 Introduction of porosity calculation using Iso-Surfaces

The following section focuses on the evaluation of the porosity. The porosity ϵ is defined by Equation 8.1:

$$\epsilon = \frac{V_{pore}}{V_{total}} \quad (8.1)$$

V_{pore} is the pore volume, V_{total} is the pore and the fibre material volume. To define the border of the total volume, different methods can be used [Mac18]. In this work, a new method is introduced using the total pressure in the sample (for big Ma numbers the entropy has to be used). The total pressure is defined in Equation 8.2. With this value it is possible to create iso volumes on the top side of the sample and on the bottom side of the sample.

$$p_{tot} = p_{stat} + p_{dyn} = p_{stat} + \rho \cdot \frac{v^2}{2} \quad (8.2)$$

$$V_{pore} = V_{box} - (V_{top} + V_{bottom}) - (V_{fibermaterial}) \quad (8.3)$$

$$V_{fibermaterial} = (V_{box} - V_{fluid}) \quad (8.4)$$

The pore volume is marked creating a iso-volume of the total pressure p_{tot} . The total pressure is the sum of the static pressure p_{stat} and the dynamic

8 Porosity

pressure p_{dyn} . Equation 8.2 shows the definition, using ρ as the air density and v as the velocity. With this variable it is possible to identify all pores in the paper web. The static pressure in the inlet is set to $1220[Pa]$, the total pressure in the outlet is set to $0[Pa]$. The velocity in the flow field is a result of the pressure distribution and the geometry of the pores in the paper web. Creating an iso-volume using the total pressure with the maximum value $1207.8[Pa]$ and the minimum $12.2[Pa]$ identifies only the void volume within the paper web, i.e. the paper pores.

$$V_{top} = -100[Pa] \leq p_{tot} \leq 12.2[Pa] \quad (8.5)$$

$$V_{bottom} = 1207.8[Pa] \leq p_{tot} \leq 1307.8[Pa] \quad (8.6)$$

$$V_{box} = 667.5[\mu m] \cdot 700.5[\mu m] \cdot 166.5[\mu m] \quad (8.7)$$

The boundary in the inlet and the outlet was set using a total pressure close to the inlet and outlet conditions. The inlet volume was created using $1207.8[Pa]$ as lower and $1307.8[Pa]$ as upper limit. The black line in Figure 8.2 shows some details. To create the lower iso-volume, the values $-100[Pa]$ to $12.2[Pa]$ have been used. Now, all required information is available to calculate the porosity using the equations Equation 8.3 and Equation 8.4. The different volumes are defined in Equation 8.5 and Equation 8.6 and Equation 8.7. The values to limit the iso-volume is 99 % on the top and 1 % on the bottom side of the pressure inlet boundary condition $1220[Pa]$. The other limits are chosen in a way to secure a capturing of all the rest of the volume inside the domain.

8 Porosity

The working process is illustrated in Figure 8.1 and Figure 8.2. An iso volume of the total pressure is a volume which contains all fluid zones within a defined minimum and maximum value.

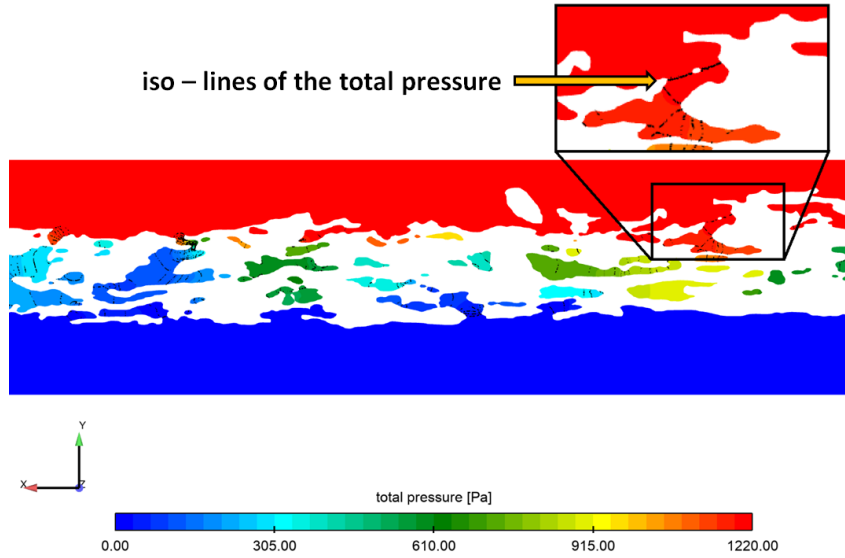


Figure 8.1: Total pressure through the sample, the black lines show the total pressure iso-lines

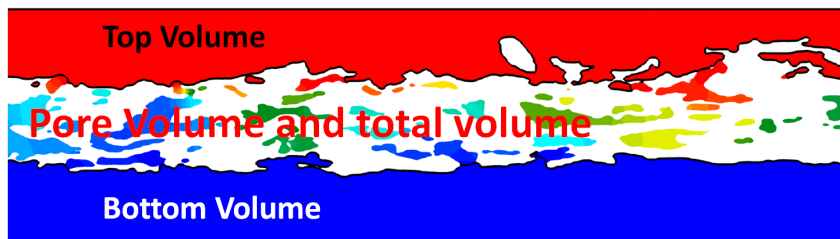


Figure 8.2: Volume fractions identified for $p_{tot} \leq 12.2[Pa]$ (Bottom Volume) and $1207.8[Pa] \leq p_{tot}$ (Top Volume)

8.2 Porosity Results using Iso-Volumes of the Total Pressure

The results can be seen in Table 8.1. The maximal porosity is 1.2 times the average porosity. The minimal porosity is 0.85 times the average. S4R1 shows 1.7 times the average flow rate and 1.2 times the average porosity. The smallest porosity was found in S2R3 with 0.84 the average value. The flow rate in this segment is the smallest with 0.45 times the average value. The result shows that the flow rate grows faster than the porosity.

Table 8.1: Porosity for 5x segmentation simulation results

Section	porosity [-]	normalized porosity	normalized flow rate
S1 R1	0.3204	1.0454	0.8825
S1 R2	0.3214	1.0487	1.2851
S1 R3	0.2684	0.8759	0.7479
S2 R1	0.2955	0.9641	1.0893
S2 R2	0.2777	0.9063	0.6874
S2 R3	0.2611	0.8522	0.4463
S3 R1	0.3192	1.0416	0.8936
S3 R2	0.3189	1.0405	1.3529
S3 R3	0.3203	1.0453	1.1181
S4 R1	0.3678	1.2001	1.6985
S4 R2	0.2942	0.9600	0.5973
S4 R3	0.3126	1.0200	1.2010
AV	0.3065	1.0000	1.0000
Min	0.2611	0.8522	0.4463
Max	0.3678	1.2001	1.6985

8 Porosity

Figure 8.3 gives the data of Table 8.1 in a diagram. R^2 is the coefficient of determination, it is the proportion of the variance in the dependent variable that is predictable from the independent variables. The normalized porosity gives $R^2 = 1$ which is to be expected, the flow rate has a smaller coefficient of determination $R^2 = 0.7447$, indicating that the flow rate is not directly linked to the porosity. The other main influence is the pore size distribution, which creates the other variance in the flow rate.

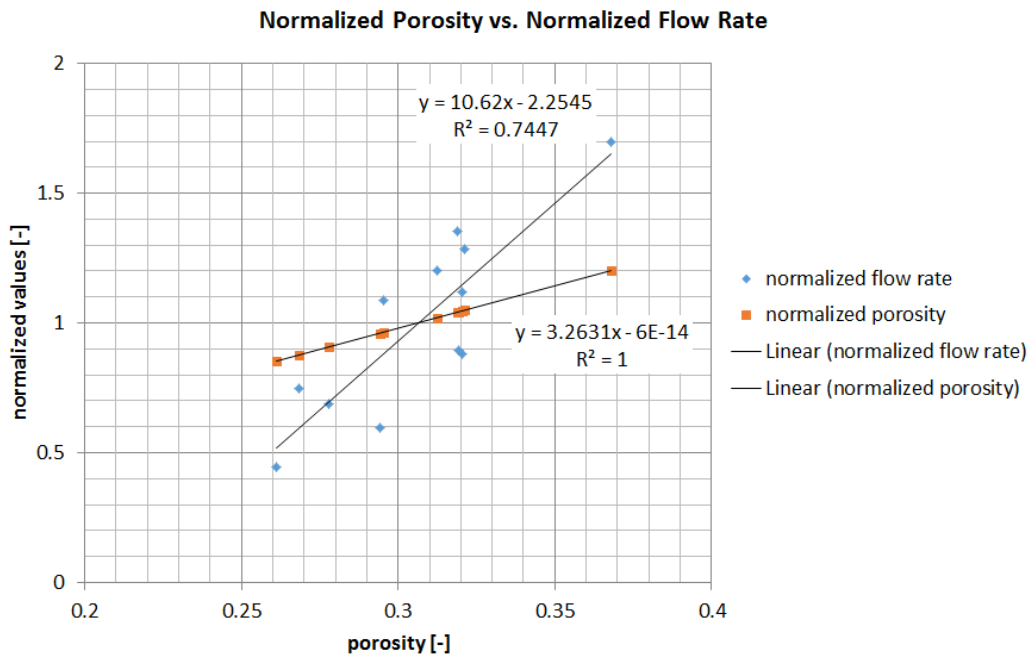


Figure 8.3: Comparison of the normalized porosity with the normalized flow rate

8 Porosity

The following images illustrate the new method:

Figure 8.4 shows the geometry of the segment S3R1 from the top. The colour indicates the paper web height in μm . The blue and cyan colour identifies regions which allow a deep look into the material.

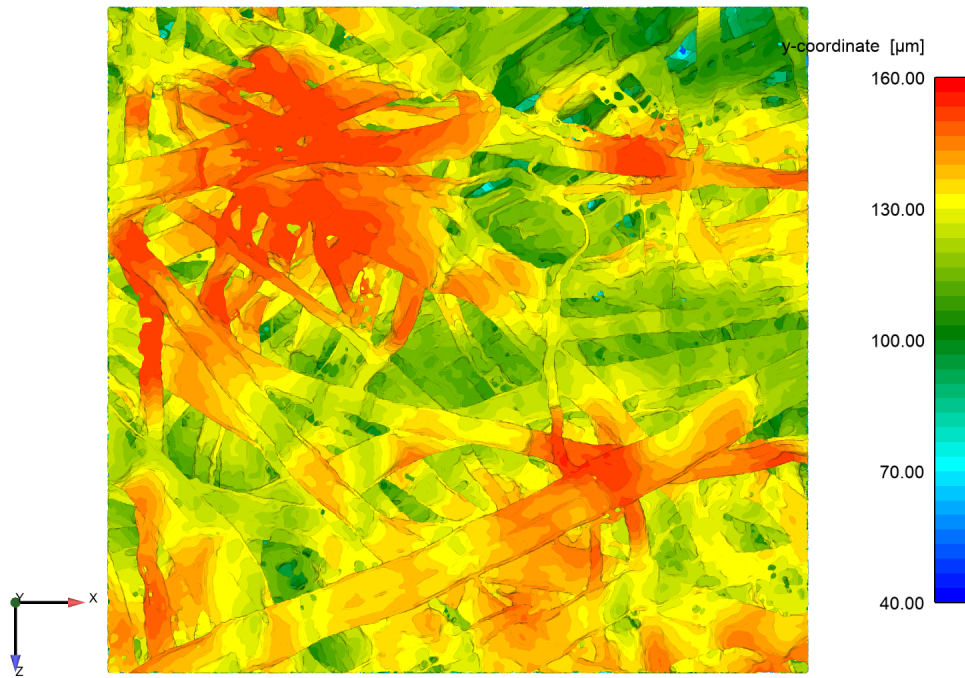


Figure 8.4: S3 R1 Top side y-coordinate [μm]

8 Porosity

Figure 8.5 shows the geometry of exactly the same segment *S3R1* also from the top. The only difference is that the image now shows the paper web with the closed pores. This image underlines the exact geometry capturing of this new method.

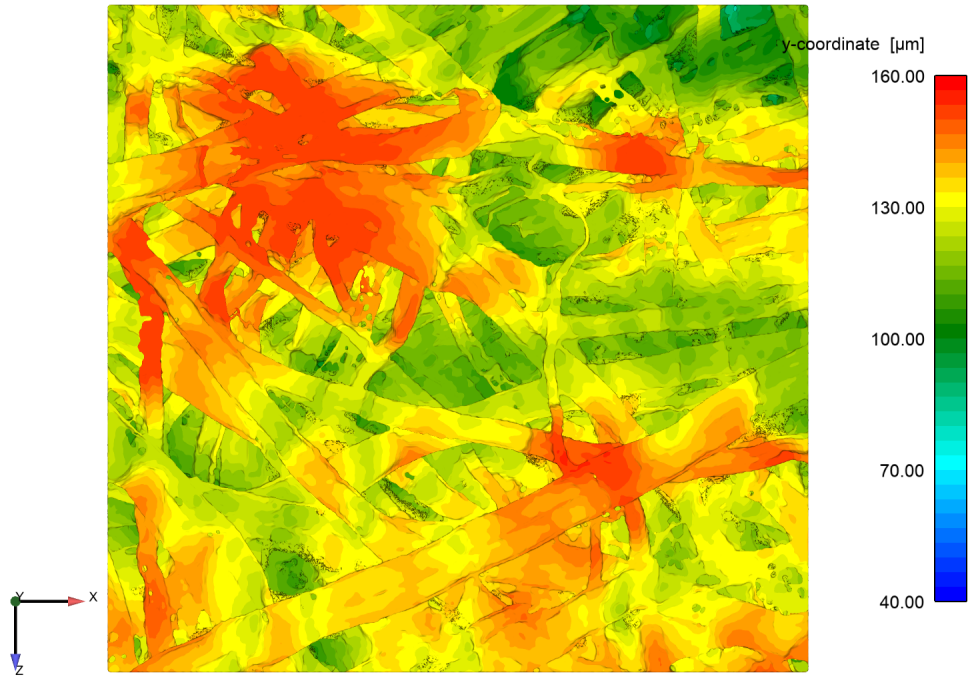


Figure 8.5: *S3 R1* top side y -coordinate [μm] of the iso volume for calculation of the porosity

8 Porosity

Figure 8.6 shows a detailed comparison of two pore zones. The left side shows the original paper web geometry containing all the pores. The right side shows exactly the same region with the pores closed using the total pressure iso-surface.

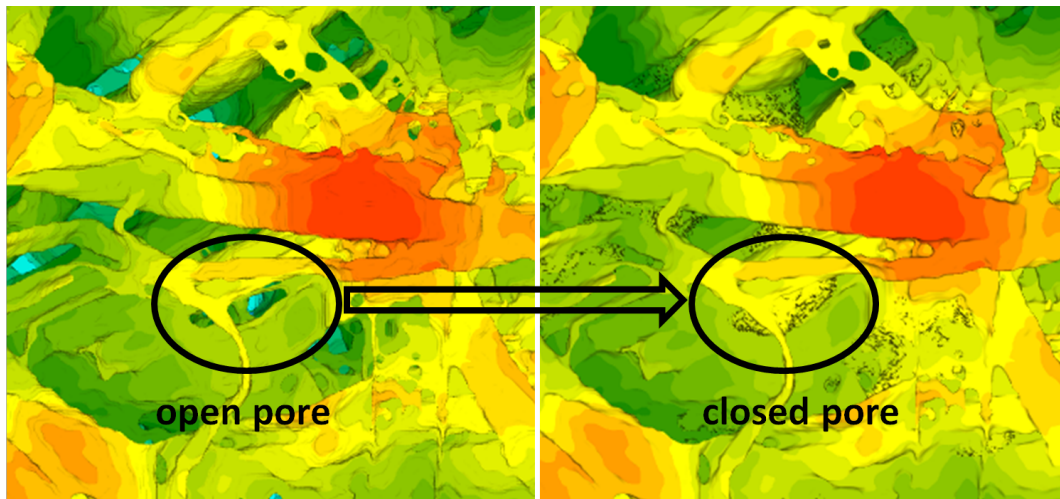


Figure 8.6: Detail of the total pressure iso-surface, pore detection mechanism

8 Porosity

Figure 8.7 shows the closed pores using the total pressure iso-surface. The pore volume is the volume which allows the air to travel through the paper web. It seems that some of the pores have a huge flat volume.

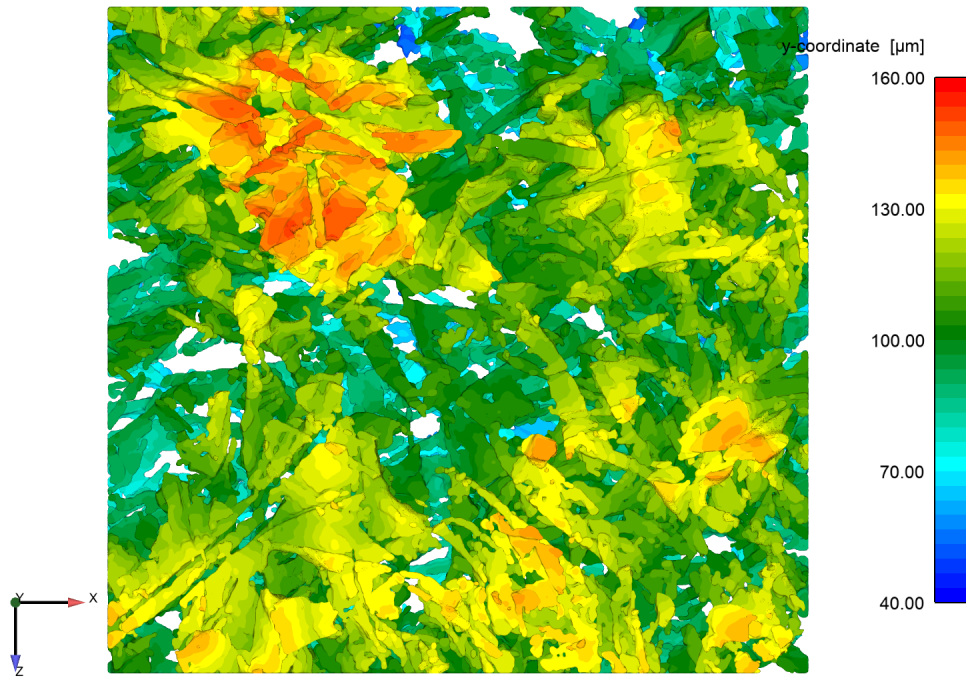


Figure 8.7: S₃ R₁ top side y-coordinate of the pores [μm]

8.3 Comparison of the Results with Carman-Kozeny-Equation

Now the results of Table 8.1 used for further analytical investigations. The Darcy-Equation Equation 8.8 gives a description of the volume flow rate $\frac{\partial V}{\partial t} = \dot{V} [m^3/s]$ based on a pressure drop Δp in $[Pa]$, an area A in $[m^2]$, the dynamic viscosity η in $[Pas]$ and a porous resistance R in $[m^2/s]$.

Darcy Equation:

$$\frac{\partial V}{\partial t} = \frac{\Delta p \cdot A}{\eta \cdot R} \quad (8.8)$$

The Carman-Kozeny-Equation gives a further description of the porous resistance R in $[m^2/s]$.

Porous Resistance:

$$R = \frac{H \cdot K \cdot (1 - \epsilon)^2}{\epsilon^3 \cdot d_p^2} \quad (8.9)$$

In Equation 8.9 H in $[m]$ is the thickness of the porous media, K in $[m^3/s]$ is a constant which has to be identified experimentally, ϵ is the porosity and d_p^2 is a characteristic particle diameter in m .

Carman-Kozeny-Equation:

$$\frac{\partial V}{\partial t} = \frac{\Delta p \cdot A \cdot \epsilon^3}{\eta \cdot H \cdot (1 - \epsilon)^2} \cdot \frac{d_p^2}{K} \quad (8.10)$$

8 Porosity

Based on the CFD results $\frac{d_p^2}{K}$ and H are calculated for all 12 segments in Table 8.2. H in $[\mu m]$ can be calculated using the upper volume Equation 8.5, the lower volume Equation 8.6 and the total volume. The area A is for all segments the same ($0.467[mm^2]$).

Table 8.2: Porosity for 5x segmentation simulation results

Section	porosity [-]	H [μm]	$\frac{d_p^2}{K}$ [m/s]
S1 R1	0.3204	74.82	5.85E+08
S1 R2	0.3214	69.28	4.39E+08
S1 R3	0.2684	71.87	3.65E+08
S2 R1	0.2955	73.86	3.51E+08
S2 R2	0.2777	72.11	4.50E+08
S2 R3	0.2611	77.59	5.11E+08
S3 R1	0.3192	70.02	6.09E+08
S3 R2	0.3189	68.54	4.09E+08
S3 R3	0.3203	72.36	4.77E+08
S4 R1	0.3678	65.90	6.04E+08
S4 R2	0.2942	67.53	6.88E+08
S4 R3	0.3126	71.70	4.07E+08
AV	0.3065	71.30	4.91E+08
Min	0.2611	65.90	3.51E+08
Max	0.3678	77.59	6.88E+08

8 Porosity

Now the analytical volume flow rates can be compared with the CFD results in Figure 8.8. Still, for all further analytical estimations the $\frac{d_p^2}{K}$ is set to be constant with the average value of $4.91E + 08$ in $[m/s]$.

The blue bar shows the CFD result of the volume flow rate, the orange bar shows the result using the local porosity ϵ and the local height H in $[\mu m]$ from each single segment. The result shows the same tendency as the CFD result.

The grey bar shows the results using the average porosity ϵ AV based on Table 8.2 and the local height H in $[\mu m]$ from each single segment.

The green bar shows the results using the local porosity ϵ and the average height H in $[\mu m]$ based on AV in Table 8.2.

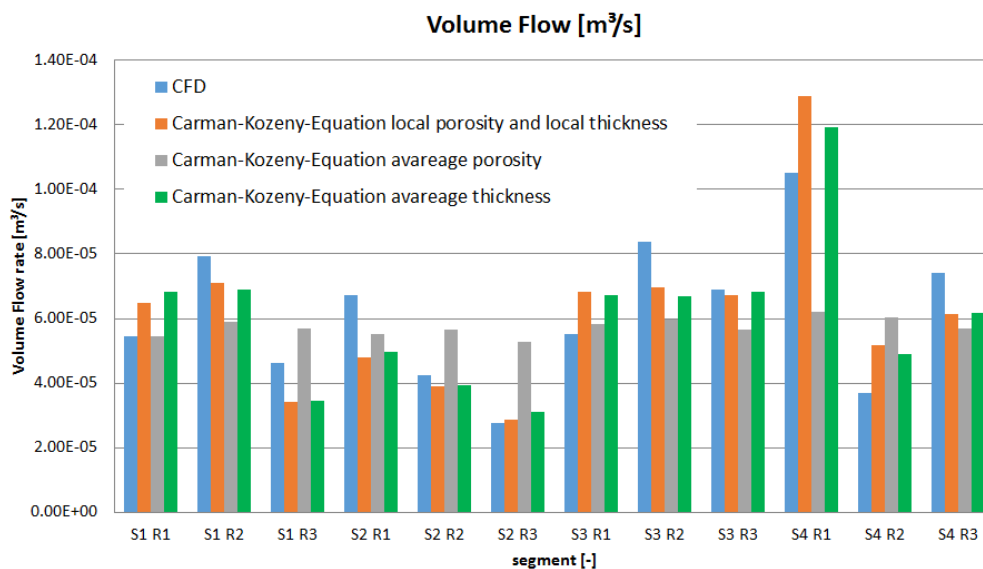


Figure 8.8: S3 R1 top side y-coordinate of the pores $[\mu m]$

The conclusion of this comparison is that the porosity ϵ has a much bigger influence on the result than the paper web thickness H . Comparing the result of the local porosity ϵ and the average paper web thickness H (green) with the CFD result (blue) gives a good accordance. It is much closer than the result of the local paper web thickness H and the average porosity ϵ (grey).

9 Results of S3 R1 in Detail

The following section focuses on one segment and shows in detail how the air travels through the paper web. Figure 9.1 shows the paper web coloured by the y-coordinate and stream lines coloured by the air velocity. The lines start at the inlet and end at the outlet.

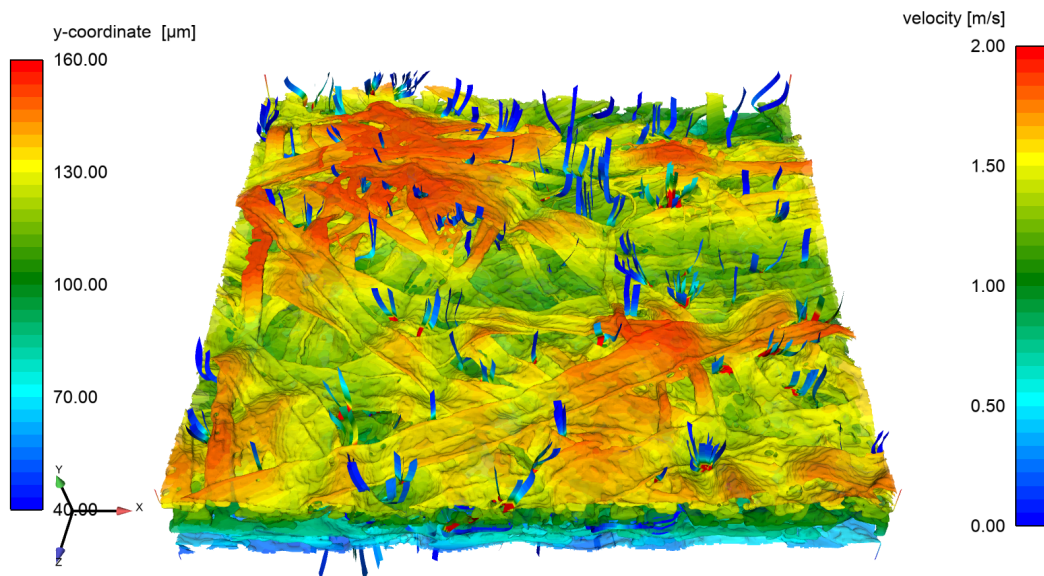


Figure 9.1: CFD Result S3 R1 stream lines through the paper web top view

9 Results of S3 R1 in Detail

Figure 9.1 shows the top view and Figure 9.2 shows the bottom view. Following the lines through the web is hard because of the complex flow pattern which can be seen in Figure 9.3, again coloured by the y- coordinate. It is evident that the airflow through paper is governed by concentrated high speed flow through a few large pores. The stream lines start randomly distributed in Figure 9.1 and they are collected in a couple of pores and leave the paper web in Figure 9.2 through a couple of pores.

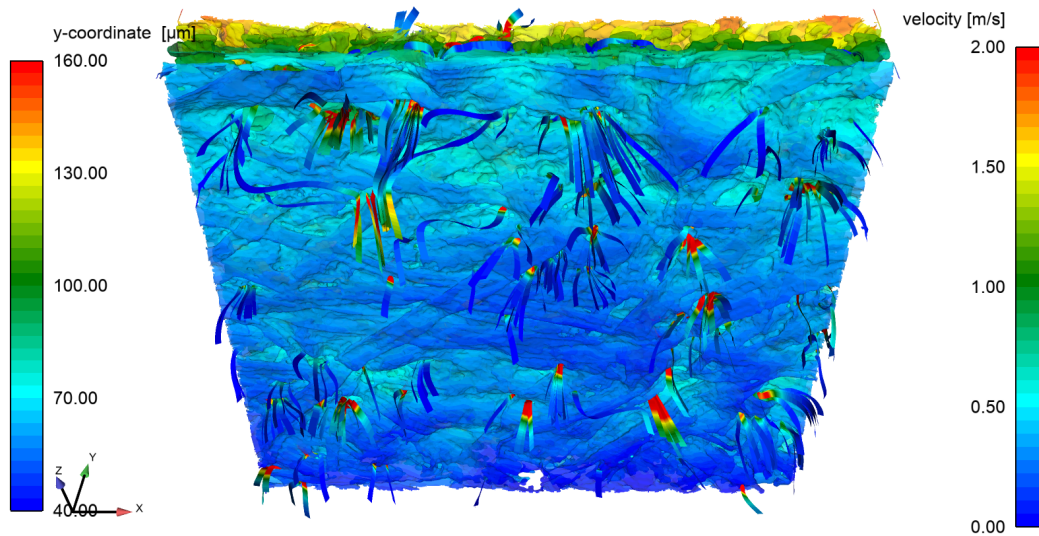


Figure 9.2: CFD Result S3 R1 stream lines through the paper web bottom view

9 Results of S3 R1 in Detail

Figure 9.3 shows the streamlines coloured with the y-coordinate in μm . This image shows how the air travels in the paper web, the green colour identifies the middle of the paper pores, using the y-coordinate.

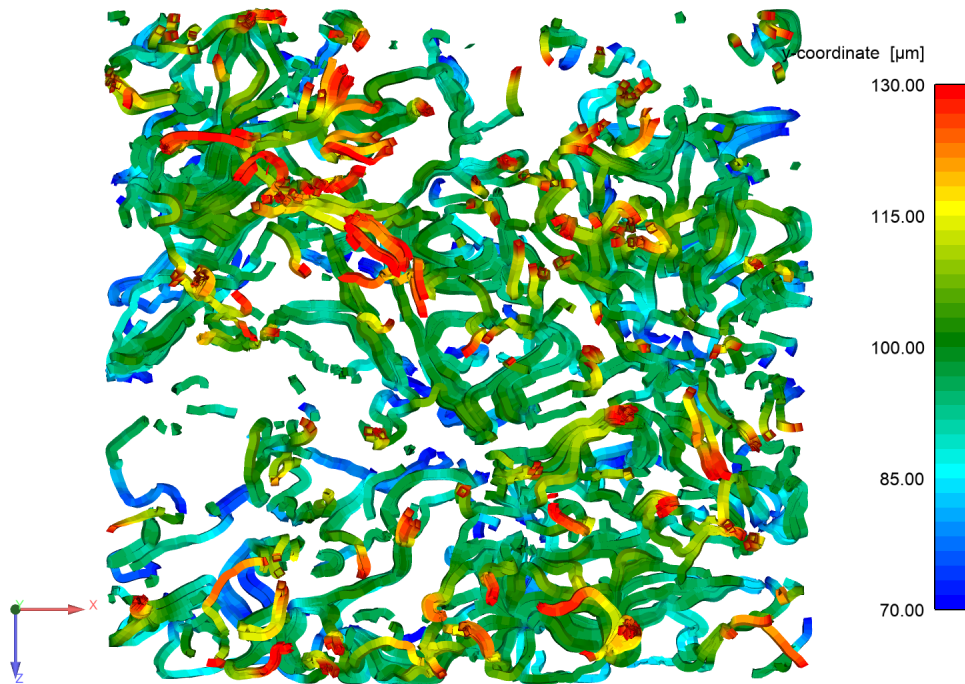


Figure 9.3: Stream lines, coloured with the y coordinate in $[\mu m]$ through the paper web

9 Results of S3 R1 in Detail

Figure 9.4 and Figure 9.5 show the static pressure and the velocity of the air in a clip through the web. The two pictures illustrate why the total pressure has to be used for marking the pores in the domain. If the static pressure would be used instead of the total pressure, the regions with a big velocity would be excluded from the iso-volume since the static pressure is small in regions with high velocity.

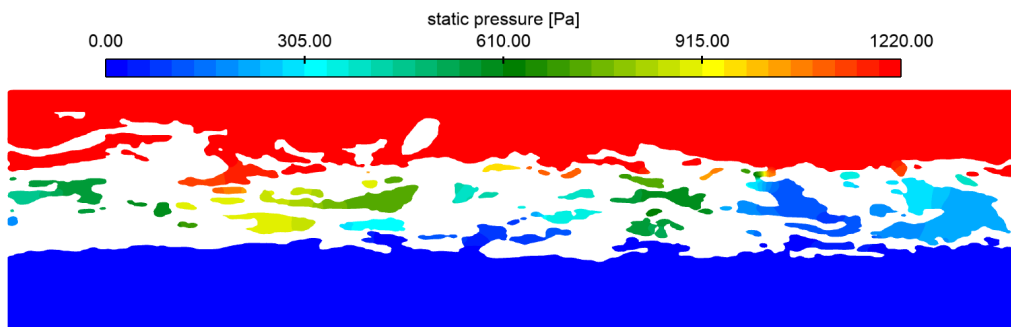


Figure 9.4: Static pressure in the z-plane

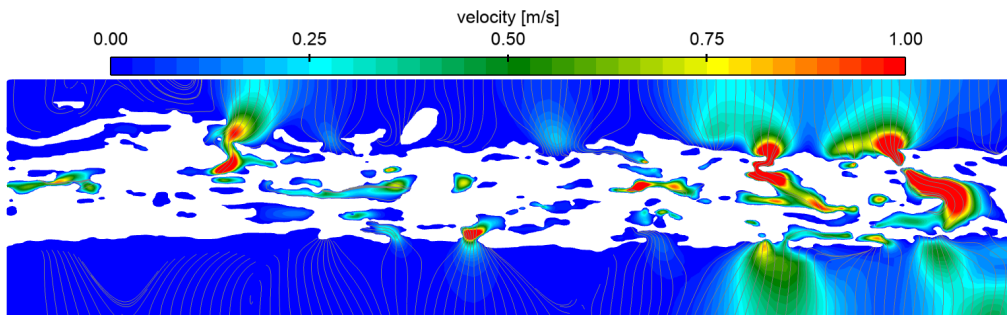


Figure 9.5: Velocity in the z-plane

9 Results of S3 R1 in Detail

Finally, those results are used to analyse the area of the pores which are responsible for most of the air flow. Figure 9.6 shows the velocity of the air in the pores. In most of the regions the velocity is zero. Figure 9.7 shows the secondary flow velocity.

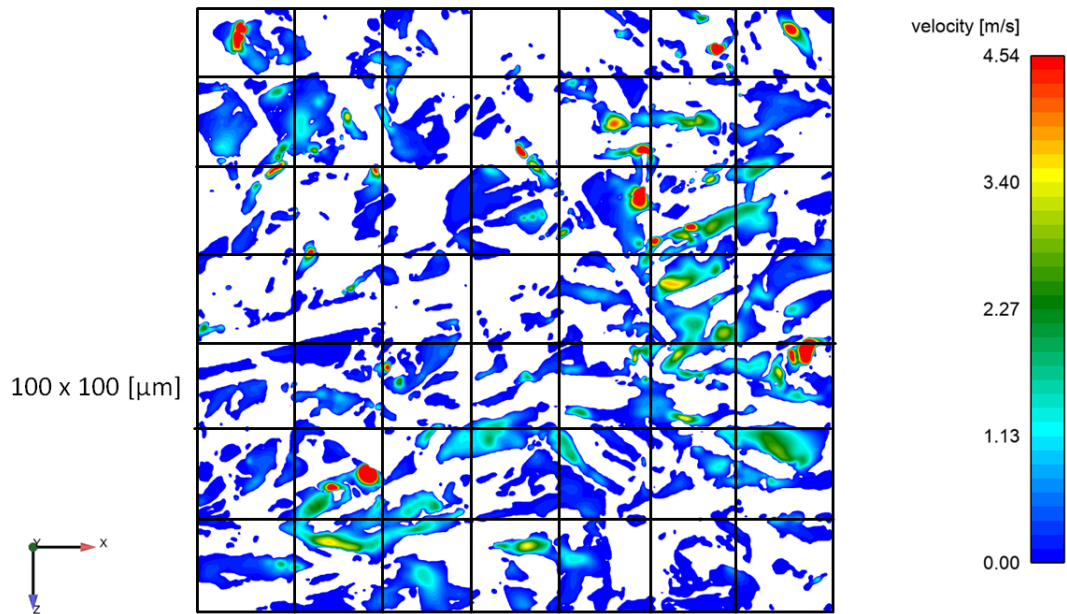


Figure 9.6: All pores in the middle of the paper web

9 Results of S3 R1 in Detail

Figure 9.7 shows the secondary flow velocity. The secondary flow is the flow in the x-z plane. The air has velocities bigger than $2[m/s]$ in the pores parallel to the paper web.

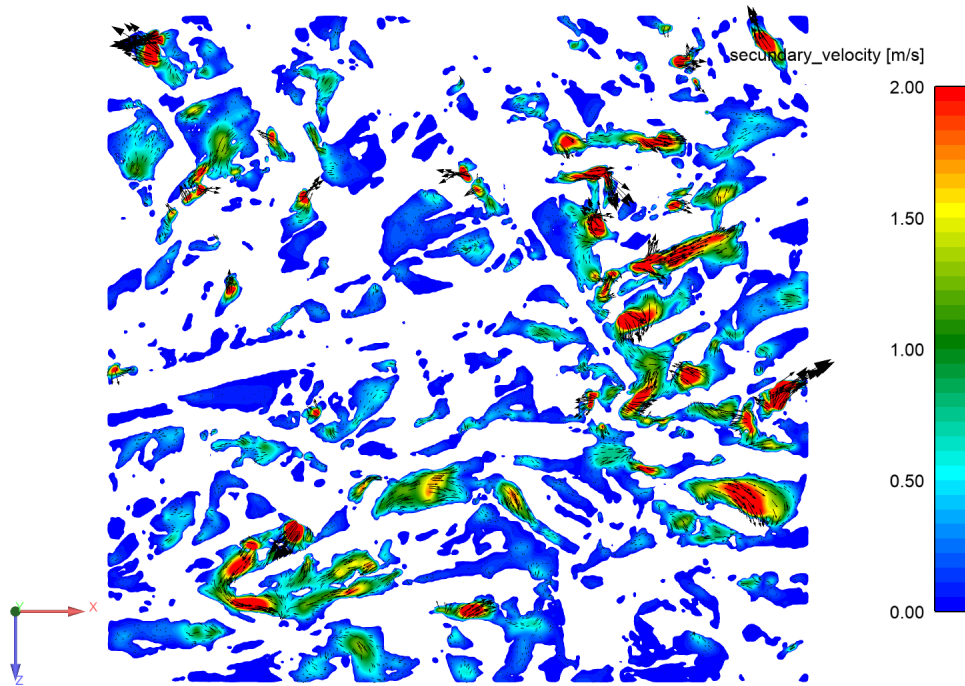


Figure 9.7: Secondary flow velocity in the pores

9 Results of S3 R1 in Detail

Showing regions with a velocity higher than $2.27[m/s]$ (which is 100 times the average Gurley velocity) the image changes to Figure 9.8. Now the flow rate and area can be analysed.

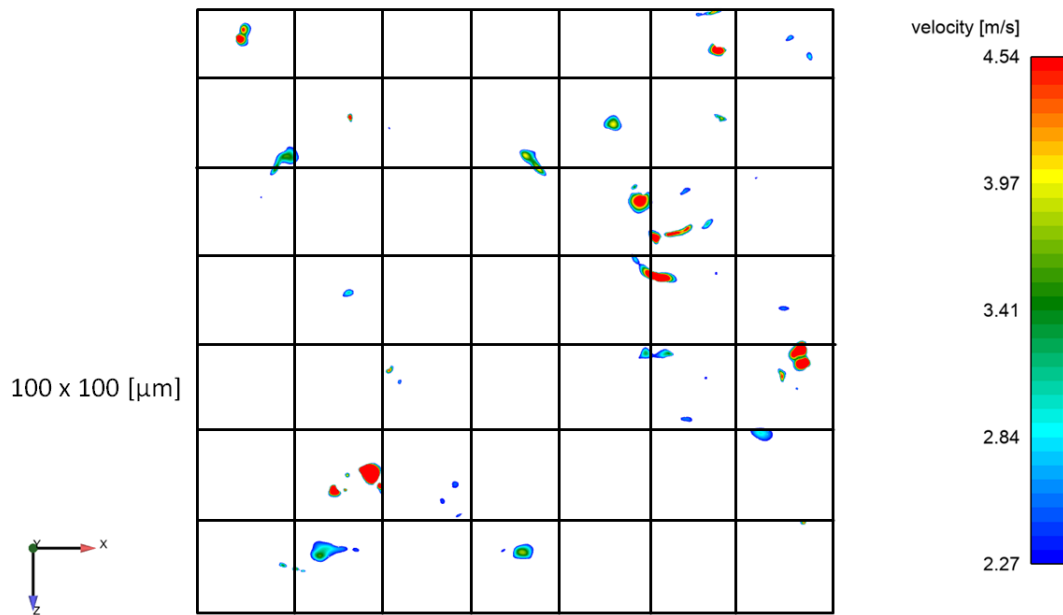


Figure 9.8: Pores responsible for 50% of the flow rate in the middle of the paper web

9 Results of S3 R1 in Detail

Table 9.1 shows the numbers in detail, 50% of the flow goes through less than 1.4% of the total sample area of the sample in the investigated paper web. The flow field is very uneven, most of the air goes through a small amount of pores. A comparison of Figure 9.6 and Figure 9.8 shows the small size of the area which is responsible for the main part of the flow rate. The black grid as reference has a mesh size of $100 \times 100 [\mu m]$. The flow channel in the pores in this clip has a diameter of about 5 to $25 \mu m$.

Table 9.1: Pore analyses, area and area weighted velocity

name of the result	area [mm^2]	velocity [m/s]	area [%]
Gurley	645.2	0.0227	-
total area S3 R1	0.4676	0.0856	100
all pores S3 R1	0.1833	0.2183	39.2
pores containing 50% of the flow S3 R1	0.0065	2.4629	1.39

9 Results of S3 R1 in Detail

Figure 9.9 shows the behaviour in detail, 50% of the flow goes through less than 5% of the pore area. Also interesting is that more than 70% of the pore area are see a secondary ore a reversed flow. This can be seen in the Figure 9.9 by the fact that the flow rate has a maximum at 108%. That shows that about 8% are reversed flow. Reversed flow has an opposite direction to the main flow direction, which follows the global pressure gradient.

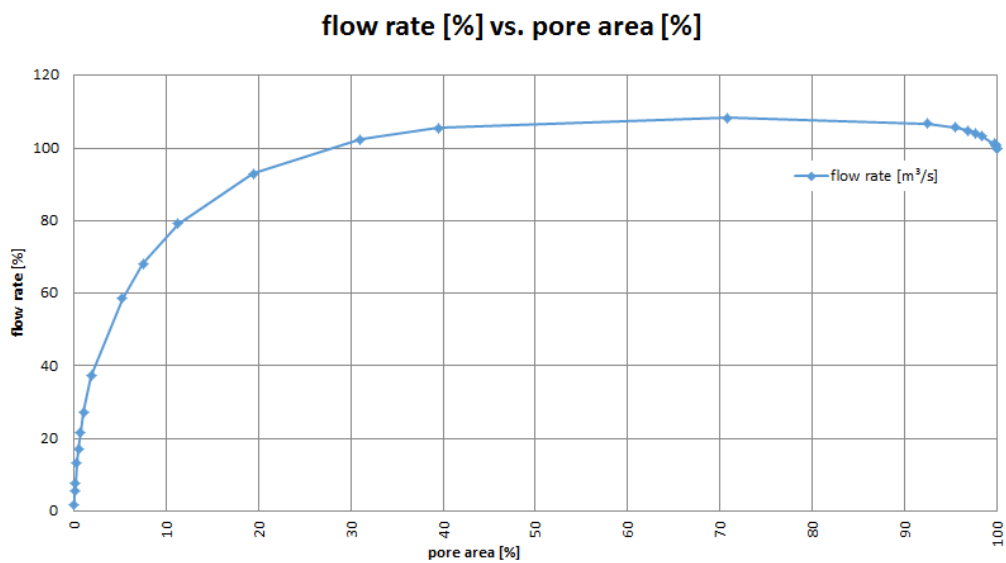


Figure 9.9: Flow rate depending on the pore area

10 Conclusion

In this work an automatized workflow was developed to convert μ -CT datasets of paper to CFD meshes for simulation of air flow through the paper structure. A paper sample with a total area of $2.8 \times 2.0 \text{ mm}^2$ has been divided into 12 subsamples, which were converted to CFD meshes. The airflow through this sample was simulated and compared to Gurley air permeability measurements made on a large sample of the same paper (645 mm^2). The results of the simulations resulted in a 4.5 times higher air flow than the Gurley measurements, which is most probably attributed to the small sampling area used for modelling.

Based on the flow simulations, a new method to evaluate the porosity of the paper has been developed. It is based on the concept of detecting the pore volume in the paper based on the total pressure drop in the simulated air flow.

Quantitative analysis of the air flow in the pore volume revealed that only a small amount of pores carries the majority of the air flow through the web. Half of the air flow travels through less than 2% of the pore volume. Air flow was found not to be directly proportional to the porosity of the paper, which is in line with the finding that the air flow is governed by few, prominent pores.

Bibliography

- [19] Fiji. <https://imagej.net/Fiji>. Dec. 2019 (cit. on p. 11).
- [Aalo4] U. Aaltosalmi. *NUMERICAL ANALYSIS OF FLUID FLOW THROUGH FIBROUS POROUS MATERIALS*. *Journal of Pulp and Paper Science*, 30:251-255, 2004 (cit. on p. 1).
- [ANS13] ANSYS. *ANSYS FLUENT Theory Guide*. 2013 (cit. on pp. 2, 30, 32).
- [Asl17] H. Aslannejad. *Study of Hydraulic Properties of Uncoated Paper: Image Analysis and Pore-Scale Modeling*. *Transport in Porous Media*, 10.1007/s11242-017-0909-x, 2017 (cit. on p. 1).
- [Bay14] Sharareh Bayat. *Direct structured finite element mesh generation from three-dimensional medical images of the aorta*. PH.D. THESIS, University of Ottawa, 2014 (cit. on p. 21).
- [E13] Moritz E. *Fast Generation of Virtual X-ray Images from Deformable Tetrahedral Meshes*. Konrad-Zuse-Zentrum fuer Informationstechnik Berlin, ZIB-Report 13-38, 2013 (cit. on p. 21).
- [Hel16] Steiner Helfried. *Hoehere Stroemungslehre und Waermeuebertragung*. Vorlesungsskriptum TU Graz, WS 2015/2016 (cit. on p. 29).
- [Kna86] G. H. Knauf. *CALCULATIONS OF AERODYNAMIC POROSITY, SPECIFIC SURFACE AREA, AND SPECIFIC VOLUME FROM GURLEY SECONDS MEASUREMENTS*. INSTITUTE OF PAPER CHEMISTRY, TECHNICAL PAPER SERIES, 1986 (cit. on pp. 1, 4).
- [Mac10] G. Mach. *A Modular Tool Chain for High Performance CFD Simulations in Intracranial Aneurysms*. Numerical Analysis and Applied Mathematics, International Conference, American Institute of Physics, CP1281 978-0-7354-0831-9, ICNAAM, International Conference, 2010 (cit. on p. 8).

Bibliography

- [Mac18] E. Machado Charry. *Pore space extraction and characterization of sack paper using μ -CT*. *Journal of Microscopy*, Vol. 00, Issue 0 2018, pp. 112, 2018 (cit. on pp. 2, 9, 12, 19, 36, 50).
- [Miy13] Shinjiro Miyawaki. *AUTOMATIC CONSTRUCTION AND MESHING OF MULTISCALE IMAGE-BASED HUMAN AIRWAY MODELS FOR SIMULATIONS OF AEROSOL DELIVERY*. PH.D. THESIS, University of Iowa, 2013 (cit. on p. 21).
- [num19] numeca. *HEXPRESS/Hybrid*. July 2019. URL: <https://www.numeca.com> (visited on 07/11/2019) (cit. on p. 23).
- [Shi14] M. Shibata. *Acquisition of capillary pore structure by X-ray CT and visualization of flow by numerical analysis*. *Advanced Materials Research*, Vol. 845 (2014) pp 163-167, 2014 (cit. on p. 8).